JCM

Scholarly, Peer-Reviewed and Fully Refereed International Research Journal

ISSN : 2583-9152

Journal of Condensed Matter

of

Condensed Matter Research Society

Vol. 02 No. 01 (2024)

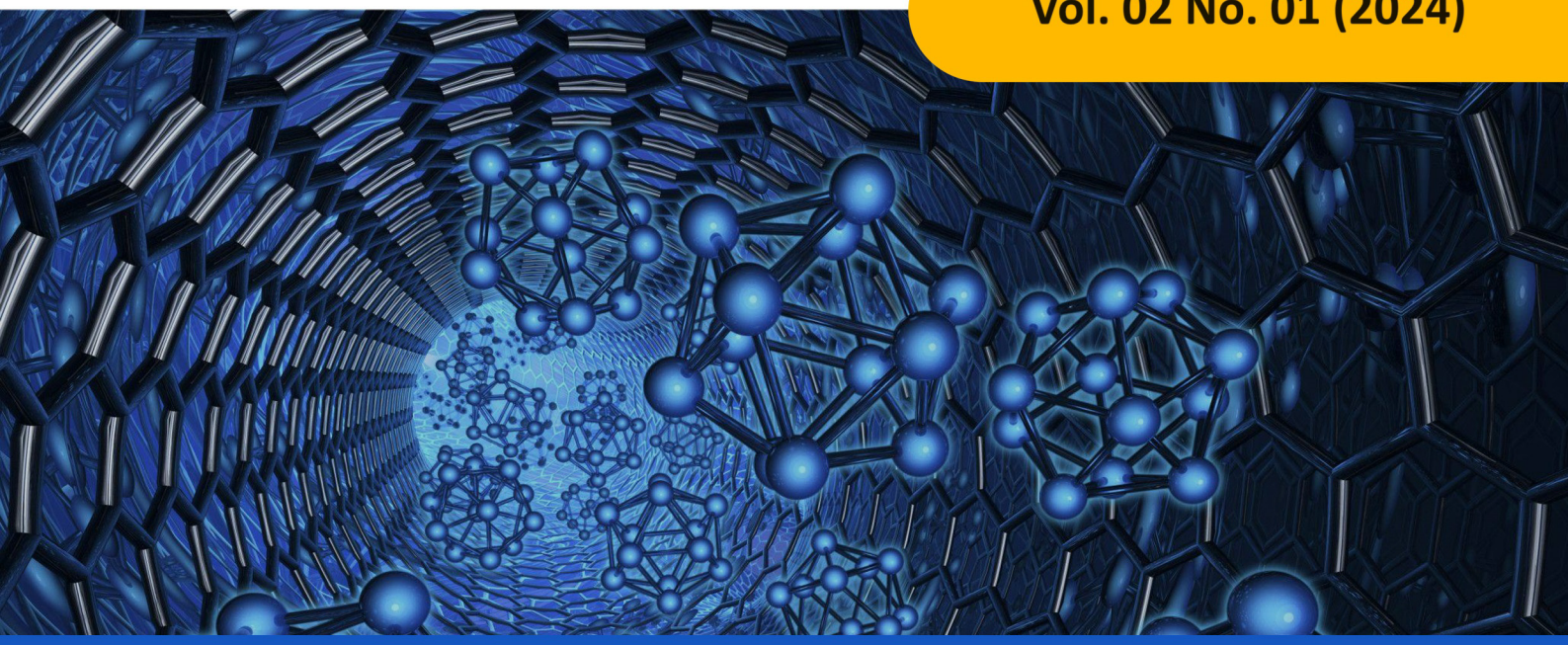

Condensed Matter Research Society

Table of Contents

Effect of Cation Disorder on Basic Parameters of $ZnFe_2O_4$ Nano-Particles Synthesized by Honey Mediated Solution Combustion Technique

Saroj Raghuvanshi

Shri Cloth Market Institute of Professional Studies, Indore, M.P., India.

raghuvanshisaroj20@gmail.com

Abstract

Nanotechnology contracts by the invention and practice of material using nanoscale dimension. Nanoscale measurement delivers nano-particles a bulky superficial area 'S' to volume ratio, hence very specific characteristics. Bulk zinc ferrite ($ZnFe_2O_4$) exhibits anti-ferromagnetism, with Néel temperature of 10K, is paramagnetic at room temperature. It has a typical spinel structure and exclusive tetrahedral - A site preference when Zn^{2+} is present, whereas Fe^{3+} ions occupy the octahedral - B site. Cationic disorder induced fractional overturn of the spinel structure, owing to partial immigration of Fe^{3+} ions from B to A site can prompt ferrimagnetism in nano zinc ferrite. Owing to the high concentration of hazardous substances and harsh conditions involved in the chemical and physical manufacturing process, a green approach utilizing fungi, bacteria, and plants has been used. Present work reports comprehensive study of the synthesis, structural and magnetic investigation of room temperature ferrimagnetism in $ZnFe_2O_4$ nanoparticles, prepared by sol gel auto-combustion mode and green synthesis method. Effect of conventional thermal annealing (ann. at 600°C for 3 hours) on magnetic properties is also reported. The magnetic and structural characteristics of synthesized and annealed $ZnFe_2O_4$ samples were determined by vibrating sample magnetometer (VSM) and X-ray diffraction (XRD). XRD verifies that the samples have formed a single-phase nano-crystalline cubic spinel configuration.

Keywords: Zn Ferrite, Green Synthesis, Cationic Disorder.
Received 13 November 2023; First Review 17 December 2023; Accepted 04 January 2024.

*** Address of correspondence**
Saroj Raghuvanshi
Shri Cloth Market Institute of Professional Studies, Indore, M.P., India

Email: raghuvanshisaroj20@gmail.com

How to cite this article
Saroj Raghuvanshi, Effect of Cation Disorder on Basic Parameters of $ZnFe_2O_4$ Nano-Particles Synthesized by Honey Mediated Solution Combustion Technique J. Cond. Matt. 2024; 02 (01): 01-05.

Available from:
https://doi.org/10.61343/jcm.v1i01.39

Introduction

Nano ferrites are being comprehensively investigated owing to their potential applications in magnetic fluids, drug delivery, magnetic refrigeration, high-density information storage, etc. [1]. Spinel ferrites have been intensively examined due to their multipurpose chemical and physical properties, due to their scientific and technical applications in photocatalysts, magnetic sensors, nano-electronics, bio-sensors, bio-medical [2]. These applications are based on the basic construction and magnetic performance of spinel ferrites which can be tailored through selecting proper preparation method. Multiple kinds of synthesis approaches including hydrothermal, sol gel, co-precipitation, electrochemical, and others have been applied for preparation of ferrite nano-particles. Cations are circulated between tetrahedral 'A', and octahedral 'B' sites in spinel ferrites, where the structural and magnetic atmospheres are rather dissimilar. Consequently, the information of the cation arrangements (on site 'A', 'B') is essential to recognize magnetic behavior of spinel ferrites. Cation distribution can be different: i) if the sample is synthesized by a particular method (owing to dissimilar preparation conditions in each method), ii) substitution by particular ions and iii) post preparation thermal treatments which can be profitably utilized to have control on structure, this will therefore impact the ferrites' magnetic characteristics. Thermal annealing would lead to changes in crystallite size as well as re-distribution of cations, leading to changes in structural and magnetic properties.

Latest developments in nano-technology are prominence on nature friendly, cost-efficient preparation methods. The green approach to nanoparticle synthesis is a non-toxic, environmentally beneficial way to synthesize nanomaterials from natural resources. Safe nanotechnology is entering a new phase because to this environmentally friendly approach. Natural honey is known as the world's oldest food source with high energy and nutritious value [3] Honey is sweet (viscous) fluid made by bees and the major

residents of honey are fructose and glucose [4]. Regular honey contains glucose and fructose, which contribute to the creation of nanoparticles that act as a natural reductant, sticky medium, and protective mediator. By using honey to prepare spinal ferrites, harmful and toxic reducing mediators are avoided during the combustion process. Special chemical properties of honey extract are used in environmentally friendly nanoparticle production. Method mediated by honey, offers a number of benefits over the traditional method that uses citric acid as a mediator.

Zinc ferrite ($ZnFe_2O_4$) is one of the most significant industrial substantial, which finds use in radio engineering, semiconductors, radio technology, and other fields. The magnetic properties of Zn ferrite nanoparticles were observed to have higher magnetization values related to the bulk materials and also the synthesis technique might also play imperative role in achieving the ferromagnetic nature of Zn ferrite [5]. Several reports on $ZnFe_2O_4$ have showed that, $ZnFe_2O_4$ is antiferromagnetic at room temperature with Néel temperature $T_N \approx 10$ K [6]. But, observed ferromagnetic nature of $ZnFe_2O_4$ synthesized by various techniques shows creation of oxygen positions in the structure. Bulk zinc ferrite have the normal spinel structure with Zn^{2+} ions occupying tetrahedral (A) site and Fe^{3+} ions being occupied in octahedral (B) site. [7]. The magnetic properties of Zn ferrites significantly depend when a small amount of Fe^{3+} ions migrate towards A site [8], therefore non-equilibrium cation distributions become a tool for tailoring magnetic properties. In this work, $ZnFe_2O_4$ spinel ferrite was synthesized using citric acid and a natural substance called honey. Further, the effects of citric acid, natural products on cation distribution, structural changes, and magnetic parameters were examined.

Sample Synthesis and Characterization

$ZnFe_2O_4$ nanopowders were prepared by a solution ignition method with acetate / citrate–nitrate pre-cursors and honey. The prepared mixture was heated to 120 degree Celsius in the air to produce "dry gel," or loose powder. The internal-combustion reaction is a heat-releasing oxidoreduction process in which nitrates mixture and honey act similarly to conventional oxidants and fuels. Samples that were prepared were annealed at 600 ºC for 3hrs to expand the degree of crystallization. Dry gel samples using critic acid and honey as fuels were labelled: citric acid as S1, honey as S2 while heat treated samples were categorized as: citric acid as S3, honey as S4. The magnetic and structural features of synthesized and annealed $ZnFe_2O_4$ samples were determined by vibrating sample magnetometer (VSM), and X-ray diffraction (XRD). Reitveld alteration software 'MAUD' (*Material Analysis Using Diffraction*) [9] was used for complete proof study of XRD patterns to calculate experimental lattice parameter ($a_{exp.}$). Distribution of Cation among varies sites was determined by XRD intensities, using Bertaut method, as described in [10]. Using the obtained cation distribution ionic radii of A-site (r_A) and B-site (r_B) (The radius of the cations are taken from the work of Shannon) [11], theoretical lattice parameter ($a_{th.}$), Oxygen positional parameter (u43m at A-site) and (u3m at B-site), the bond angles ($\theta_1, \theta_2, \theta_3, \theta_4, \theta_5$), and surface area ($S$) were calculated as described in [12 -14].

Grain size is obtained by strongest diffraction peak [311], by using Scherrer's formula,

$$D = \frac{0.9\lambda}{\beta Cos\,\theta}$$

Where β - Line width, λ - Wavelength of x-ray used, θ - Peak position (in 2θ scale).

For plane [311], the Lattice parameter (a_{exp}) was computed using the formula,

$$a_{\exp.} = d\sqrt{h^2 + k^2 + l^2}$$

Where d - Inter planner distance, (h, k, l) - Miller indices.

Following equation was used to compute the X-ray density (ρ_{xrd}),

$$\rho_{XRD} = \frac{8M}{N_A a_{\exp.}^{\ 3}}$$

Where N_A – Avagrodo's Number, M – Molecular weight, a_{exp} – Lattice parameter.

Calculation of Specific surface area (S) was done by using formula,

$$S = \frac{6}{D \times \rho_{XRD}}$$

Where D - grain diameter, ρ_{XRD} - x-ray density.

The hopping distance for site A and B (L_A and L_B)

$$L_A = \frac{a\sqrt{3}}{4} \qquad L_A = \frac{a\sqrt{2}}{4}$$

Where a_{exp} – Lattice constant.

Following formula was used to get cation distribution,

$$\frac{I_{hkl}^{abs}}{I_{h'k'l'}^{abs}} = \frac{I_{hkl}^{calc}}{I_{h'k'l'}^{calc}}$$

Where I_{hkl}^{obs} - experimental and I_{hkl}^{cal} - calculated intensities for reflection (hkl).

Results and Discussion

The representative rietveld refined XRD plot shown in figure 1 for the selected $ZnFe_2O_4$ composition (S3) of the

annealed sample. XRD patterns for prepared S1, S2 and annealed S3, S4 samples support single phase cubic spinel structure formation, ascribed honey and citric acid both plays the role of good chelating agent. Annealed (600 °C for 3hrs.) $ZnFe_2O_4$ samples support single phase formation (secondary phase not present) of nanodimensional cubic spinel (Fd3m space group) structure, attributed as role of thermal treatment support the development of spinel phase. The structural factors: Scherrer's grain dimension (*D*), x-ray density (ρ_{XRD}), and specific surface area (*S*) of as prepared and heat-treated samples calculated by examining XRD data, are showed in table-1. Grain size of as prepared samples (S1, S2) range between 22.84 – 32.52 nm, where grain size of annealed samples (S3, S4) range between 53.37 – 61.71 nm evidently illustrates formation of nano-dimensional spinel ferrite. Grain size of annealed samples (S3, S4) rises as compared to as-prepared (S1, S2) samples is ascribed to result of heat treatment that supports grain growth of the samples. Variation in *D* of the studied samples with citric acid and honey is attributed to the effect of reaction condition, which favors the formation of new nuclei preventing further growth of particles [15]. Figure 2 depicts the change of experimental (using XRD data), theoretical lattice space ($a_{exp.}$, $a_{th.}$) of dry gel and annealed samples. The observed changes in $a_{exp.}$, a_{th} of samples S1 – S4 can be ascribed to the performance of fuel (citric acid and honey), which help to relocation of Zn^{2+} and Fe^{3+} ions having dissimilar ionic radius, which alter the microstructure of sample. The excellent surface-to-bulk ratio of nano ferrites makes them a vital component in improving the performance of solid catalysts. Specific surface area *(S)* is an inversely correlated with both Scherrer's grain diameter *(D)* and x-ray density (ρ_{XRD}). Particles specific surface area is the summation of the areas of the exposed surfaces of the particles per unit mass. [16]. Specific surface area of the studied samples (S1, S2, S3, S4) varies from 18.15 – 48.64 m^2/g. For sample S1, the high specific surface area value and low D value obtained make it a better option for the purpose of catalysis.

XRD analysis was used to determine the cation dispersal, which is shown for each sample in the second table. It is noteworthy fact, Zn ferrite displays normal spinel structure. The Zn^{2+} and Fe^{3+} ions' occupation of sites A, and B provides a clear picture of the cation distribution of the materials under study. According to the closely matched $a_{exp.}$, a_{th}, the estimated and real distribution of cations between the sites A and B agree extremely well. In the present work, the non-magnetic Zn^{2+} ions (zero magnetic moment) are dispersed at both A, B sites which is responsible for relocation of magnetic Fe^{3+} ions reside on site B. A precise depiction of the function of the natural extract and citric acid is reflected in obtained cationic distribution.

Table 1: X-ray density (ρ_{XRD}), surface area (S), Grain diameter (D) of Zn ferrite.

Sample	D (nm)	ρ_{XRD} (Kg/m^3)	S (m^2/g)
S1	22.84	5400.1	48.64
S2	32.52	5365.2	34.39
S3	53.37	5350.7	21.01
S4	61.71	5357.1	18.15

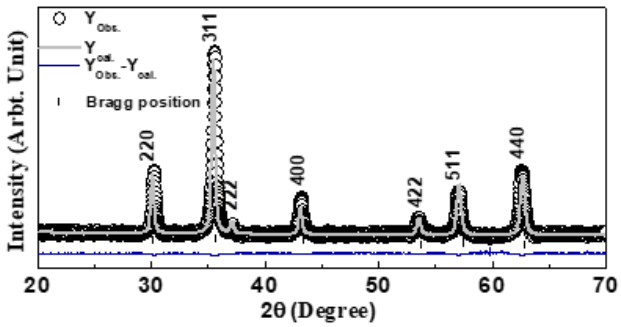

Figure 1: XRD pattern of nano sized zinc ferrite

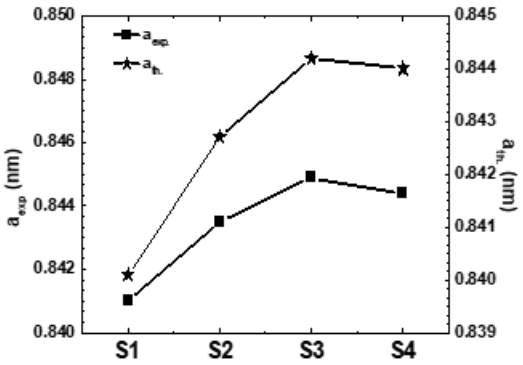

Figure 2: Variation of a_{exp} and a_{th}

Observed results shows noticeable variation in XRD and cation distribution parameters like Oxygen positional parameter (u43m at A-site) and (u3m at B-site), ionic radii of A-site (r_A) and B-site (r_B), hopping length for A-site (L_A) and B-site (L_B), *(see table 2)*, bond positions (θ_1, θ_2, θ_3, θ_4, θ_5) *(see table 3)*. Oxygen position parameter u43m for tetrahedral site range between 0.3816 – 0.3857 and u3m at B-site is range between 0.2566 – 0.2607 (shown in table 2). It ought to be pointed out that u43m and u3m is a measurement for the sample's disorganisation, and its standard value of u43m is 0.375 (not any disarray in the lattice). Experimental values of oxygen position parameter for all calculated specimens are in excess of the real value indicating that the spinel's tetrahedral and octahedral sites are distorted. Variation of r_A, and r_B correspondingly spans between 0.054 nm – 0.60 nm, and 0.65 nm – 0.68 nm. Observed changes in r_A and r_B values of studied samples show the variation of distance between tetrahedral and

octahedral cation-anion.

Table 2: Cation distribution, changes in ionic radii of A-site (**r_a**) and B-site (**r_b**), hopping length for site A and B (L_A and L_B), Oxygen positional parameter (u43m at site -A) and (u3m at site- B), of $ZnFe_2O_4$ system.

Cation Distributions	r_a (nm)	r_b (nm)	U43m	U3m	L_a (nm)	L_b (nm)
S1 $(Zn_{0.41}\ Fe_{0.59})^A[\ Zn_{0.59}Fe_{1.41}]^B$	0.054	0.067	0.3816	0.2566	0.3638	0.2970
S2 $(Zn_{0.55}\ Fe_{0.45})^A[\ Zn_{0.45}Fe_{1.55}]^B$	0.056	0.068	0.3825	0.2578	0.3642	0.2973
S3 $(Zn_{1.0})^A[Fe_{2.0}]^B$	0.060	0.065	0.3857	0.2607	0.3649	0.2983
S4 $(Zn_{0.9}\ Fe_{0.1})^A[\ Zn_{0.1}Fe_{1.9}]^B$	0.059	0.065	0.3850	0.2599	0.3647	0.2978

Hoping length for sites A and B (L_A, L_B) are depicted in table 2, Changes that were noticed in hopping length for site A and B of studied specimens is similar to that of the variation of experimental lattice parameter.

The total strength of the magnetic exchanges (A-B, B-B, and A-A) is determined by the bond length and bond angles between the cations and cation-anion. Bond length is inversely correlated with strength (exchange cooperation), but directly connected to bond angle. Changes in bond angles among A–O–B (θ_1, θ_2), B–O–B site (θ_3, θ_4) and A–O–A site (θ_5) in the examined specimens is illustrate in table 3, suggests about the magnetic interaction among A and B sites cations. Obtained highest value of bond angles θ1, θ2, θ_5 and lowest value of bond angles θ_3, θ_4 for S1 indicates weakening of the B–B relationship and rising of A–B, A–A interaction in comparison of the other samples.

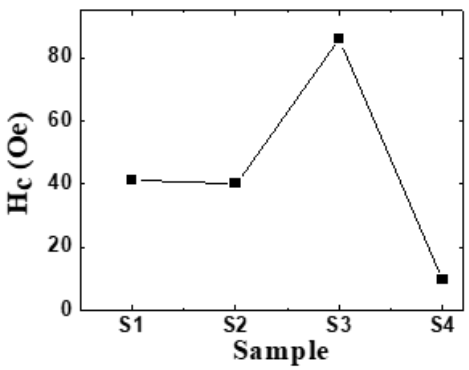

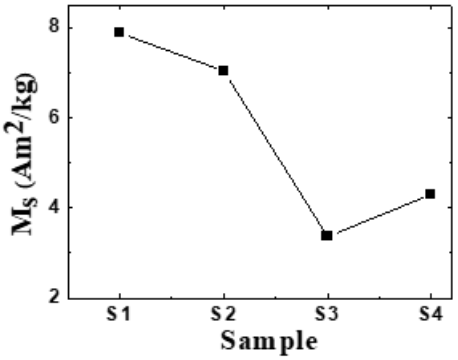

Figure 3: (a) Variation of coercivity (H_c), **(b)** Variation of saturation magnetization (M_s)

Figure 3 (a) and 3 (b) respectively depicts the variation of coercivity (H_c) and saturation magnetization (M_s) of the examined specimens. Coercivity values of samples range between 09.54 – 86.00 Oe. Perusal of Fig. 3(a) shows that highest value of H_c for sample S3 suggests effect of heat treatment. Figure 3 (b) depicts variation of experimental M_s (at 300 K) of studied samples. Highest Ms of 7.89 Am^2/kg was calculated for the as-burnt S1 sample in contrast to other samples, whereas annealed sample S3 gives value of M_s is 3.37 A m^2/kg. It should be mentioned that the results obtained with honey and citric acid are a result of the Fe and Zn ions' varying friction on the sites A, B. (table 2). Obtained changes in cation distribution (on A, B site) increases alteration (u) within the spinel system which is amply demonstrated by detected deviations in M_s, shows the significance of cationic dispersion in influencing determining magnetic characteristics.

Table 3: Changes in bond angles (**(A-O-B)** θ_1, θ_2, **(B-O-B)** θ_3, θ_4, **(A-O-A)** θ_5) of $ZnFe_2O_4$ system.

Sample	θ_1 (°) (A-O-B)	θ_2 (°) (A-O-B)	θ_3 (°) (B-O-B)	θ_4 (°) (B-O-B)	θ_5 (°) (A-O-A)
S1	123.142	144.107	93.155	125.981	73.961
S2	123.082	142.716	93.860	125.352	73.190
S3	121.865	138.865	95.218	126.429	70.635
S4	122.082	139.716	94.860	126.352	71.190

Conclusion

In summary, $ZnFe_2O_4$ nanoparticles are made by using a simple sol-gel auto combustion process that uses honey and citric acid as combustibility. The structural phase development of $ZnFe_2O_4$ spinel ferrite nanoparticles was demonstrated by the x-ray diffraction investigation. Cation distribution confirmed the migration of Zn element, Fe ions in mutually tetrahedral and octahedral sites in synthesized $ZnFe_2O_4$. Grain size, structural alterations, and cation distribution are observed to have a notable effect on the magnetic properties of zinc ferrite nanoparticles. The cation dispersal and grain size effect were discovered to cause changes in magnetic characteristics such as coercivity and saturation magnetization.

Acknowledgement

I would like to acknowledge my guide Prof (Dr.) S. N. Kane, Magnetic Materials Laboratory, SOP, DAVV, Indore, with my sincerest respect and gratitude, who not only introduced me to this area of **Nanocrystalline Ferrites** but also explained the finer aspects with a lot of patience and determination throughout.

References

1. D Peddis, N Yaacoub, M Ferretti, A Martinelli, G Piccaluga, A Musinu, C Cannas, G Navarra, J M Greneche, D Fiorani, Phys.: Cond. Matter, 23:426004, 2011.
2. H Agarwal, S Venkat Kumar, and S Rajeshkumar, Resource Efficient Technologies, 3: 406–413.2017.
3. D Philip, Spectrochim. Acta A Mol. Biomol. Spectrosc., 73(4):650–653, 2009.
4. E R Balasooriya, C D Jayasinghe, U A Jayawardena, R W D Ruwanthika, R M de Silva, and P V Udagama, Journal of Nanomaterials, Vol. 2017:5919836, 2017.
5. C E R Torres, F Golmar, M Ziese, P Esquinazi, and S P Heluani, Phy. Rev. B, 84:064404, 2011.
6. L Raghavan, G Pookat, H Thomas, S Ojha, D K Avasthi, and M R Anantharaman, J. Magn. Magn Mater., 385:265–271, 2015.
7. H Ohnishi, and H T Teranishi, J. Phys. Soc. Jpn. 16:35–43, 1961.
8. L Weil, E F Bertaut, and L Bochirol, J. Phys. Radium, 11:208, 1950.
9. L Lutterotti and P Scardi, J. Appl. Cryst., 23(4):246–252, 1990.
10. L Gastaldi, and A Lapiccirella, J. Sol. Stat. Cham., 30:223–229, 1979.
11. R D Shannon, Acta Cryst., A32:751, 1976.
12. J Smit, and H P J Wijn, Ferrites, New York: Wiley-Inter Science 1959.
13. K E Sickafus, J M Wills, and N W Grimes, J. Am. Ceram. Soc., 82:3279–3292, 1999.
14. X Qi, J Zhou, Z Yue, Z Gui, and L Li, Mater. Sc. and Eng. B, 99:278–281, 2003.
15. R S Yadav, I Kuritka, J Vilcakova, J Havlica, J Masilko, L Kalina, J Tkacz, J Švec, V Enev, and M Hajdúchov, Adv. Nat. Sci.: Nanosci. Nanotechnol, 8:045002 (14pp), 2017.
16. Z X Tang, C M Sorensen, K J Klabunde and G C Hadjipanayis, Phy. Rev. Letters, 67:3602–3605, 1991.

Impact of Incident Angle on Defect Modes in Symmetric and Asymmetric One-Dimensional Photonic Crystals

Vipin Kumar[a] and Ravinder Kumar

Department of Physics, Janta Vedic College, Baraut (U.P.), India-250611

[a] vipinphys@gmail.com

Abstract

Our study has meticulously explored how the angle of incidence influences defect modes in one-dimensional photonic crystals (PCs) with a central defect. We focused on two types of PCs - those with symmetric and asymmetric configurations, each incorporating a single defect. In asymmetric PCs, we observed a unique defect mode occurring precisely at the central wavelength. In contrast, symmetric PCs displayed two separate defect modes near the central wavelength. We discovered that expanding the defect layer allows these two modes to converge into a unified central defect mode. It is important to note, though, that the intensities of these combined modes are distinct from those in asymmetric PCs. The transfer matrix method is employed to examine the propagation traits of the structures we proposed.

Keywords: Defects, Transfer matrix method, Transmittance.
Received 08 January 2024; First Review 13 January 2024; Accepted 22 January 2024.

*** Address of correspondence**
Dr. Vipin Kumar
Department of Physics, Janta Vedic College,
Baraut (U.P.), India-250611

Email: vipinphys@gmail.com

How to cite this article
Vipin Kumar and Ravinder Kumar, Impact of Incident Angle on Defect Modes in Symmetric and Asymmetric One-Dimensional Photonic Crystals, J. Cond. Matt. 2024; 02 (01): 06-10.

Available from:
https://doi.org/10.61343/jcm.v2i01.48

Introduction

Since the pioneering work of Yablonovitch and John, the study of electromagnetic characteristics in photonic crystals – artificially engineered structures with periodic variations in dielectric constants – has been a focal point of research [1-17]. These studies have shown how periodic changes in dielectric functions significantly alter the spectral properties of electromagnetic waves. In such structures, the electromagnetic spectrum shows distinct allowed and forbidden bands of photonic energy, akin to the electronic bands in periodic potentials. This has led to the recognition of these materials, characterized by periodic dielectric modulation, as photonic band gap (PBG) materials [18]. Intriguingly, fundamental optical properties like band structure, reflectance, group velocity, and spontaneous emission rates can be manipulated by varying the dielectric function's spatial distribution [4, 5].

One-dimensional photonic crystals (1D PCs) are notable for their array of applications, such as dielectric mirrors, low-loss waveguides, optical switches, filters, and limiters. Both theoretical and experimental research confirms that 1D PCs possess absolute omnidirectional PBGs [19-23]. While pristine PCs are functional, doped or defective versions offer enhanced versatility. Semiconductor doping significantly broadens their application scope. The analogy between electromagnetism and solid-state physics has led to investigations into band structures in periodic materials and the emergence of localized modes within the band gap due to lattice defects. These doped photonic crystals show resonant transmission peaks within the band gap, indicative of localized states [24], resulting from changes in the interference patterns of incident waves. Modifications to introduce defects into pristine PCs include altering layer thicknesses [25], adding new dielectrics [26], or removing specific layers [27, 28].

The incorporation of defect states in photonic crystals, especially in two-dimensional (2D) and three-dimensional (3D) PCs, has attracted significant interest due to their vast applications. In 2D and 3D PCs, point defects can create microcavities, line defects can act as waveguides, and planar defects as perfect mirrors [29, 30]. Similarly, introducing defect layers in 1D PCs results in localized defect modes within the PBGs. Given the easier fabrication of 1D PCs compared to their 2D and 3D counterparts, these defective modes can be efficiently integrated into 1D PCs for various applications, including optical filters and splitters, light-emitting diodes, and lasers [31-33].

In this communication, we focus on the theoretical analysis of defect mode properties in different materials, examining these defect modes using the transfer matrix method.

Theoretical Analysis

Figure 1 depicts a schematic diagram of a one-dimensional photonic crystal incorporating a defect.

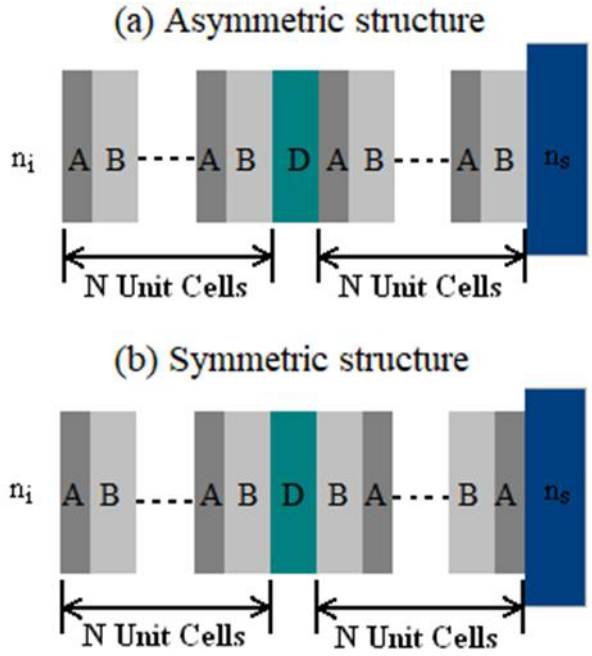

Figure 1: Schematic diagram of 1-D Photonic crystal (a) Asymmetric structure (b) Symmetric structure.

Our study examines two types of structures: asymmetric and symmetric, where 'H' and 'L' denote materials with high and low refractive indices, respectively. To determine the transmission spectrum, we utilize the transfer matrix method (TMM) [34]. Within this method, we can express the transfer matrix for each layer as follows:

$$Z_j = X_j \Upsilon_j X_j^{-1}; \quad (1)$$

In this context, 'j' represents either the H or L layers, and the terms 'X_j' and 'Υ_j' refer to the dynamical matrix and the propagation matrix, respectively. The dynamical matrix for different polarizations can be defined by the following equations:

$$X_j = \begin{pmatrix} 1 & 1 \\ n_j \cos\alpha_j & -n_j \cos\alpha_j \end{pmatrix} \text{ for TE mode} \quad (2)$$

$$\text{and } X_j = \begin{pmatrix} \cos\alpha_j & \cos\alpha_j \\ n_j & -n_j \end{pmatrix} \text{ for TM mode} \quad (3)$$

Also, the propagation matrix 'Υ_j' can be expressed by the following relation:

$$\Upsilon_j = \begin{pmatrix} e^{i\beta_j} & 0 \\ 0 & e^{-i\beta_j} \end{pmatrix} \quad (4)$$

Where β_j is called phase and can be expressed in terms of refractive index (n_i), thickness of the layer (d_i) and wavelength (λ) of the incident wave as:

$$\beta_j = \frac{2\pi d_j}{\lambda} n_j \cos\alpha_j \quad (5)$$

For the two types of PCs considered in this study, the transfer matrix expressions can be written as:

$$Z = \begin{pmatrix} Z_{11} & Z_{12} \\ Z_{21} & Z_{22} \end{pmatrix} = X_0^{-1} (Z_A Z_B)^N Z_D (Z_A Z_B)^N X_0$$

for asymmetric PC (6)

$$Z = \begin{pmatrix} Z_{11} & Z_{12} \\ Z_{21} & Z_{22} \end{pmatrix} = X_0^{-1} (Z_A Z_B)^N Z_D (Z_B Z_A)^N X_0$$

for symmetric PC (7)

The transmission coefficient, based on the matrix elements presented in equations (6 & 7), can be expressed as follows:

$$t = \frac{2\delta_i}{(Z_{11} + \delta_f Z_{12})\delta_i + (Z_{21} + \delta_f Z_{22})} \quad (8)$$

In this expression, $\delta_{i,f}$ is defined as $n_{i,f}(\cos\alpha_{j,f})$ for the TE polarized wave and as $(\cos\alpha_{j,f})/n_{i,f}$ for the TM polarized wave. Here, the subscripts 'i' and 'f' refer to the values in the medium of incidence and the medium of emergence, respectively. Meanwhile, the transmittance of the structure can be determined by the following:

$$T = \frac{\delta_f}{\delta_i} |t|^2 \quad (9)$$

In the following section, we will calculate the transmission spectra using equation (9), focusing on the photonic crystal with a defect as illustrated in Figure 1.

Results and Discussion

Consider a conventional photonic crystal denoted as "air/(AB)^{16}/Substrate," known for its photonic band gap in the ultraviolet and visible regions. For this investigation, B is identified as TiO_2, characterized by a refractive index (n) of 2.34867, while A is represented by MgF_2 with an n value of 1.3855. MgF_2 is a particularly suitable material for photonic crystals due to its unique characteristics, including absorption commencing below 115nm and a refractive index close to unity. As the substrate, SiO_2 (n=1.46) is employed. The thickness of layers A and B in Figure 1, adheres to the condition of the quarter-wavelength, specifically, $n_A d_A = n_B d_B = \lambda_0/4$, where λ_0 designates the wavelength under consideration, set at 350nm for this study.

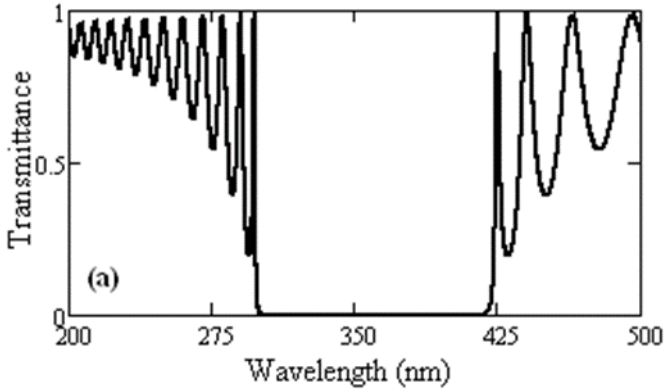

Figure 2: Transmission spectra of Air/(HL)^{16}/SiO_2 structure

Figure 2 illustrates the transmittance of this structure, as computed using Equation (9). It is evident from Figure 2 that a comprehensive band gap is present in the vicinity of the design wavelength, which is 350nm. The main objective of the present numerical computation is to introduce a defect in the middle of this structure, both symmetrically and asymmetrically, and subsequently investigate the defect modes in both configurations.

Case 1: Symmetric Structure [Air/$(HL)^8D(HL)^8$/SiO_2]

In the context of the asymmetric structure, we have presented transmission spectra for various defect materials, considering SiO_2 (n=1.46), Al_2O_3 (n=1.66574), BGO (n=2.13), and ZnS (n=2.58789), at different angles of incidence (0º, 20º, 40º, & 60º). These transmission spectra are illustrated in Figures 3 to 6. Notably, these figures reveal a notable trend: as the angle of incidence increases, the defective modes gradually shift towards the lower boundary of the forbidden band gap. Furthermore, the intensity of these defect modes diminishes as the angle of incidence increases. It's worth noting that this decrease in intensity is particularly pronounced for defect materials with refractive indices that closely approach $(n_H-n_L)/2$.

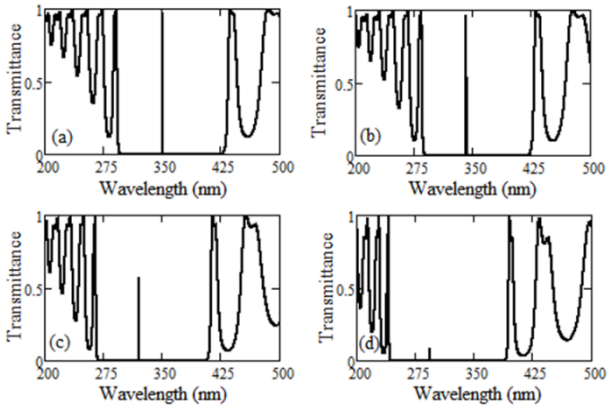

Figure 3: Transmission spectra of Air/$(HL)^8D(HL)^8$/SiO_2 structure for D=SiO_2 @different incident angles (a) 0º (b) 20º (c) 40º (d) 60º.

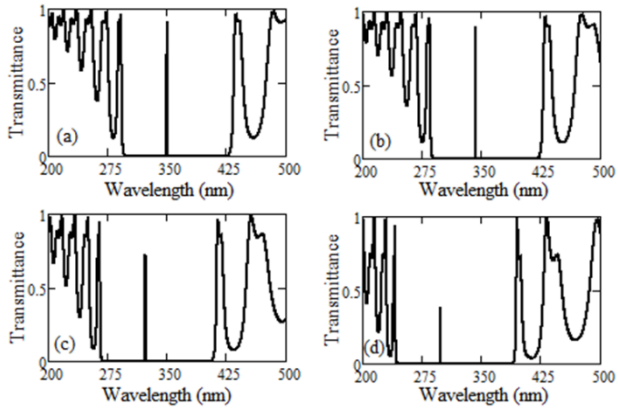

Figure 4: Transmission spectra of Air/$(HL)^8D(HL)^8$/SiO_2 structure for D=Al_2O_3 @different incident angles (a) 0º (b) 20º (c) 40º (d) 60º.

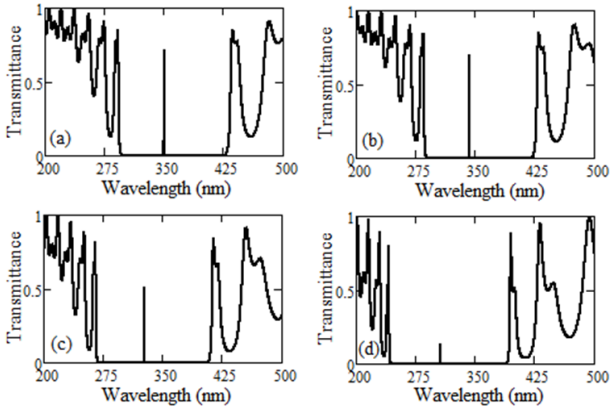

Figure 5: Transmission spectra of Air/$(HL)^8D(HL)^8$/SiO_2 structure for D=BGO @different incident angles (a) 0º (b) 20º (c) 40º (d) 60º.

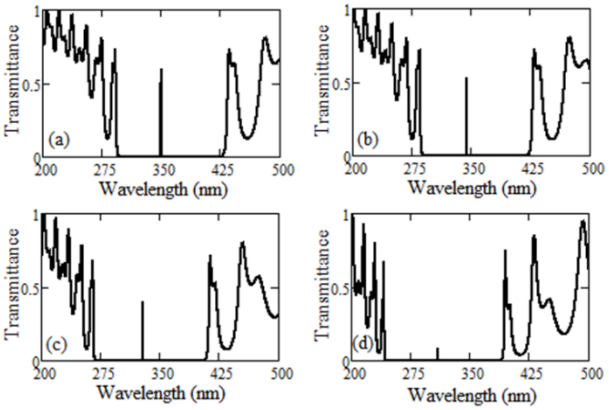

Figure 6: Transmission spectra of Air/$(HL)^8D(HL)^8$/SiO_2 structure for D=ZnS @different incident angles (a) 0º (b) 20º (c) 40º (d) 60º.

Case 2: Symmetric Structure [Air/$(HL)^8D(LH)^8$/SiO_2]

In the scenario of the symmetric structure, we have displayed transmission spectra for various defect layers, including SiO_2, Al_2O_3, BGO, and ZnS, featuring a defect thickness of $d_D= \lambda_0/4n_D$.

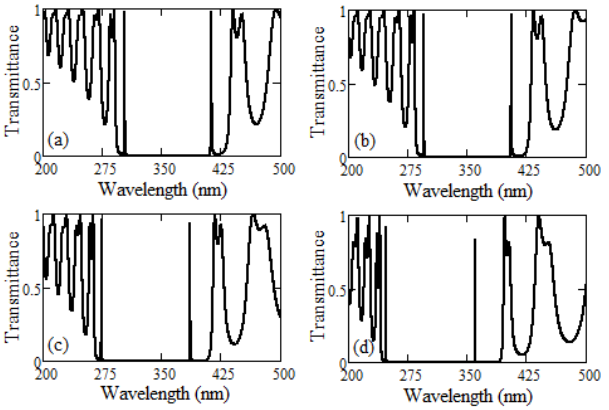

Figure 7: Transmission spectra of Air/$(HL)^8D(LH)^8$/SiO_2 structure for D=SiO_2 @different incident angles (a) 0º (b) 20º (c) 40º (d) 60º.

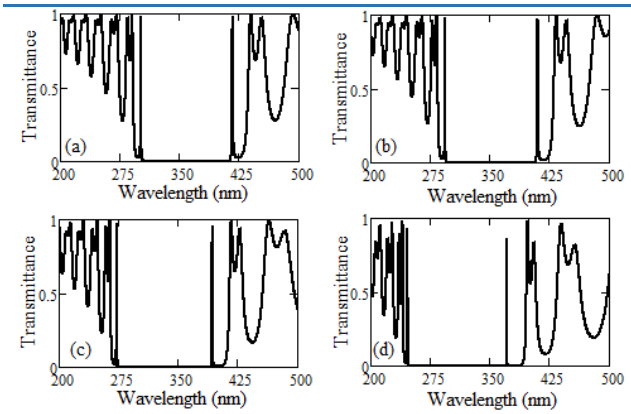

Figure 8: Transmission spectra of Air/$(HL)^8D(LH)^8/SiO_2$ structure for D=Al_2O_3 @different incident angles (a) 0º (b) 20º (c) 40º (d) 60º.

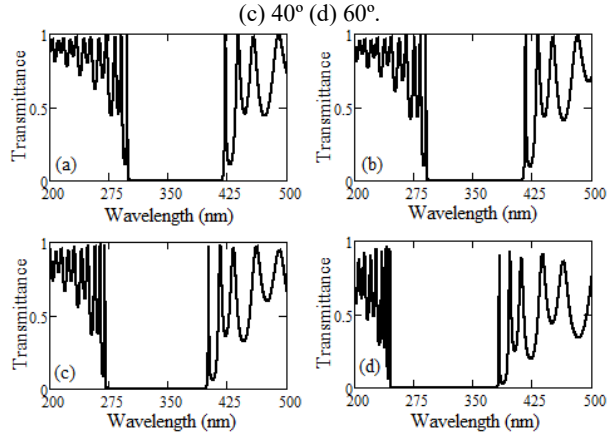

Figure 9: Transmission spectra of Air/$(HL)^8D(LH)^8/SiO_2$ structure for D=BGO @different incident angles (a) 0º (b) 20º (c) 40º (d) 60º.

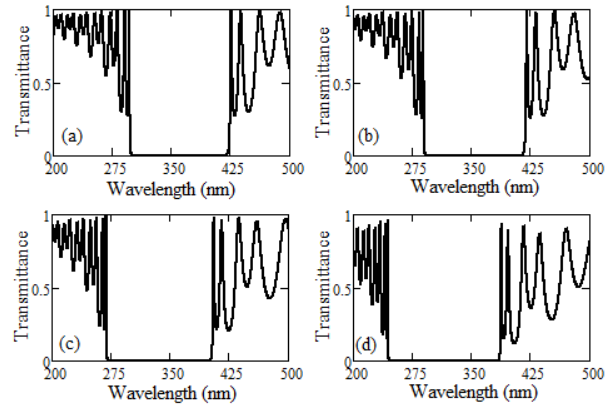

Figure 10: Transmission spectra of Air/$(HL)^8D(LH)^8/SiO_2$ structure for D=ZnS @different incident angles (a) 0º (b) 20º (c) 40º (d) 60º.

These spectra are presented at different angles of incidence (0º, 20º, 40º and 60º) and are visualized in Figures 7-10. These figures clearly show that in this configuration, two defect modes are noticeable near the edges of the photonic band gap (PBG) when the incidence angle is normal. As the angle of incidence increases, the defect mode on the left disappears, and the one on the right moves towards the left. Furthermore, as the refractive index of the defect layer increases, both defect modes gradually disappear. It's also observed that the intensity of these defect modes diminishes with a higher angle of incidence.

Notably, the behaviour of these defect modes differs from the asymmetric case. These two defect modes essentially disappear when the material ZnS is employed, primarily because its refractive index closely approximates that of the H material. Therefore, by deliberately incorporating defects in a symmetric or asymmetric fashion, we can effectively create either one or two defect modes as needed. This approach allows for the tailored design and fabrication of photonic devices to meet specific requirements.

Conclusion

This research delves into the influence of the angle of incidence on defect modes within a one-dimensional photonic crystal (PC) that features a central defect. The investigation focuses on two distinct configurations of photonic crystals: symmetric and asymmetric. In the case of asymmetric PCs, we observe that a defect mode emerges exactly at the central wavelength. This is contrasted with symmetric PCs, where two separate defect modes are identified near the central wavelength. Interestingly, when the defect layer is expanded in symmetric PCs, these two defect modes coalesce into a singular mode at the central wavelength. However, it's important to note that the intensities of this merged mode differ significantly from those observed in the asymmetric PCs. This study not only contributes to a deeper understanding of the behavior of photonic crystals under varying conditions but also provides valuable insights that could be instrumental in the design and development of advanced photonic devices, where control over such defect modes is crucial for achieving desired optical properties and functionalities.

References

1. E Yablonovitch. *Phys. Rev. Lett.*, 58:2059, 1987.
2. K M Ho, C T Chan and C M Soukoulis. *Phys. Rev. Lett.*, 65:3152, 1990.
3. J D Jonopoulos, P Villeneuve and S Fan. *Nature*, 386:143 1997.
4. J A M Rojas, J Alpuente, J Pineiro and R Sanchez, *Prog. Electromagn. Res.*, PIER 63:89 2006.
5. E Yablonovitch and T J Gmitter, *Phys. Rev. Lett.*, 63:1950 1989.
6. J D Joannopoulos, R D Meade and J N Winn, *Photonic Crystals: Molding the Flow of Light*, Princeton Univ. Press, Princeton, NJ, 1995.
7. E Burstein and C Weisbuch, *Confined Electron and Photon: New Physics and Applications*, Plenum Press, New York, 1995.
8. G Du, X Zhou, C Pang, K Zhang, Y Zhao, G Lu, F Liu and A Wu, S. Akhmadaliev, S. Zhou et al., *Adv. Opt. Mater.*, 8:2000426 2020.
9. A K Goyal, A Kumar and Y Massoud, *Crystals*, 12:992 2022.
10. A T Jervakani and B S Darki, *Opt. Commun.*, 526:128884 2023.
11. L Dan, D S Citrin and S Hu, *Opt. Mater.*, 109:110256 2020.

12. E Shahram, M Azardokht, K M Hossein, O Sareh, G Elham and H Mohsen, *Photon. Netw. Commun.*, 31:516 2016.
13. T Hiroya, T Isamu, F Hisayoshi and I Hideo, *J. Lightwave Technol.*, 36(12):2517 2018.
14. X Chen, H Ni, D Zhao and Y Wang, *Appl. Opt.*, 61(26):7786-7792 2022.
15. N Kumar, S Kaliramna and M Singh, *Silicon*, 14:6933 2022.
16. N Kumar and J Saraf, *Optik*, 252:168577 2022.
17. A Kumar, N Kumar and K B Thapa, *Eur. Phys. J. Plus*, 133:250 2018.
18. C Soukoulis, *Photonic Band Gap Materials*, 71–79, Kluwer Academic, Dordrecht, 1996.
19. J P Dowling, *Science* 282:1841 1998.
20. E Yablonovitch, *Opt. Lett.* 23:1648 1998.
21. D N Chigrin, A V Lavrinenko, D A Yarotsky andS V Gaponenko, *Appl. Phys. A: Mater. Sci. Process.* 68:25 1999.
22. B Suthar, V Kumar, Kh S Singh and A Bhargava, *Opt. Commun.* 285(6):1505-1509 2012.
23. V Kumar, Kh S Singh, S K Singh and S P Ojha, *Prog. Electromagn. Res.*, PIER M 14:101-111 2010.
24. G Guida, A de-Lustrac and P Priou, *Prog. Electromagn. Res.,* PIER 41:1 2003.
25. B Suthar and A Bhargava, *IEEE: Photon. Tech. Lett.,* DOI:10.1109/LPT.2011.2178401.
26. C M Soukoulis, Photonic band gaps and localization, NATO ARW, Plenum Press, New York, 1993.
27. D R Smith, R Dalichaouch, N Kroll and S Schultz, *J. Opt. Soc. Am.,* 10(2):314 1993.
28. V Kumar, Kh S Singh and S P Ojha, *Optik*, 122:1183-1187 2011.
29. J D Joannopoulos, R D Meade and J N Winn, Photonic Crystal: Molding Flow of Light, Princeton Univ. Press, Princeton, 1995.
30. H Y Lee and T Yao, *J. Appl. Phys.*, 93:819 2003.
31. Z M Jiang, B Shi, D T Zhao, J Liu and X Wang, *Appl. Phys. Lett.*, 79:3395 2001.
32. M W Feise, I V Shadrivov and Y S Kivshar, *Phys. Rev. E*, 71:037602 2005.
33. W D Zhou, J Sabarinathan, P Bhattacharya, B Kochman, E W Berg, P C Yu and S W Pang, *IEEE: J. Quantum Electron,* 37:1153 2001.
34. P Yeh, Optical Waves in Layered Media, John Wiley and Sons, New York,1988.

Mg Doped Zno Nanostructures: Application as an Environmental Photo-Catalyst

Shakshi Chauhan[1,a], Jyoti Gahlawat[1], Parveen Bhatt[1], Kaushlya Sihag[2]

[1] *Department of Physics, Baba Mastnath University, Rohtak (Haryana), India.*
[2] *Department of Physics, School Education, Panchkula (Haryana), India.*

[a] chauhanshakshi912@gmail.com

Abstract

In this era, metal oxide nanoparticles with appliances in solar, catalysis, sensors, actuators, and many other fields, are highly sought-after because of their wide band gap. This study examines the Mg doped ZnO nanoparticles for the structural, electrical transportation and photo-catalytic behaviour. The XRD, FT-IR (Infrared Spectroscopy), PL (Photoluminescence), and Complex Impedance Spectroscopy were used to characterise the prepared sample. The wurtzite hexagonal structure in space group P63mc was shown by the XRD data. The analyzed crystallite sizes, planner distances, and cell volumes of Mg doped ZnO nanoparticles are 35.2 nm, 2.6122 Å, and 60.91 Å^3, respectively. The aggregation in sample is visible in the micrographs. The PL spectra was traced at an excitation wavelength of 330 nm (λ) using a PL spectrometer. Using the FTIR approach, IR spectra with acmes about 520–640 cm^{-1} were traced, leading to Zn–O bond stretching. Using a photocatalytic reactor, the photocatalytic degradation of magnesium-doped ZnO nanoparticles was measured for two hours. For the Mg doped ZnO sample, the degradation efficiencies (η%) is 67 percent.

Keywords: Zinc Oxide, Mg, Photo-luminescence, Visible light, Photo-catalytic.
Received 02 February 2024; First Review 05 March 2024; Accepted 25 March 2024

*** Address of correspondence**
Shakshi Chauhan
Department of Physics, Baba Mastnath University, Rohtak (Haryana), India

Email: chauhanshakshi912@gmail.com

How to cite this article
Shakshi Chauhan, Jyoti Gahlawat, Parveen Bhatt, Kaushlya Sihag, Mg Doped Zno Nanostructures: Application as an Environmental Photo-Catalyst, J. Cond. Matt. 2024; 02 (01): 11-16.

Available from:
https://doi.org/10.61343/jcm.v2i01.40

Introduction

A new class of devices, including spin light-emitting diodes, spin field effect transistors, catalytic devices, spin-based quantum computers, and memory systems, is being developed by the combination of heavier spin and charge [1-4]. Because of their potential application in spintronics devices, where the spin and charge of the electrons can be applied mutually, photocatalysis—which is created by doping a semiconductor with a small amount of transition metals - has drawn a lot of attention. In addition, photocatalysis holds promise for a number of technological advancements, including non-volatility, increased data processing speed, lower electronic power utilisation, water purification, and higher integration densities when compared to other semiconductors [2,5]. The implementation of this kind of catalytic application is still a contentious issue because of the material's poor magnetic characteristics. All aspects of Mn-doped II–V and III–V compound semiconductors have been thoroughly studied. For data storage, ferromagnetism at room temperature is one of the most crucial properties. One of the main challenges for semiconductor spintronics devices is the discovery of appropriate magnetic semiconducting materials that will successfully allow spin-polarized carriers to be injected, transported, and modulated. Diluted magnetic semiconductors with cations that match the valence of common magnetic ions like magnesium, such as CdMnTe and ZnMnSe, have been the subject of numerous investigations. The II–VI oxide semiconductor zinc oxide (ZnO) exhibits a straight and broad band gap (3.37 eV), good transparency, long-term stability, and a high exciton binding energy (almost 60 meV at room temperature) [6-12]. It has received careful scrutiny due to its superior optoelectronic, sensing, and photocatalytic characteristics. Numerous technological uses come to an end with it, such as photocatalysts, resistive switching devices, lasers, sensors, light emitting diodes, solar cells, and, most recently, spintronics. Similar to ZnS nanoparticles, it displays strong room temperature luminescence capabilities; however, it might be enhanced by using ZnO/ZnS nanocomposites or the ZnS:Mn/ZnO nanocrystals core shell [6, 12-15]. Numerous techniques, including sol–gel, hydrothermal, chemical synthesis, chemical vapour deposition, thermal evaporation, and others, have been used to produce modified ZnO nanoparticles and thin films. In

this study, we looked at how the temperature during calcinations affected the structural, optical, and photocatalytic characteristics of magnesium-modified ZnO.

Experimental Detail

In the current work, preparatory materials were derived from $Zn(CH_3COO)_2$ (zinc acetate dehydrate), $MgCl_2$ (magnesium chloride), NaOH (Sodium hydroxide), C_2H_5OH (ethanol), and DI water. No additional purification was required. Zinc acetate dehydrate and sodium hydroxide were used as the stoichiometric ratio preparatory precursors or materials for the conformist co-precipitation synthesis of magnesium modified ZnO nanoparticles (referred to as Mg-ZnO (0.04)). After that, these precursors were dissolved in a mixture of DI water and ethanol. After then, the mixture of these precursors was disturbed for a whole hour at 80 °C. This solution was then allowed to place overnight before being repeatedly cleaned with DI water and dried in an oven program to 80 ˚C for 12 hours. The resulting powder was then annealed for four hours at 450 °C and examined using a variety of characterization methods, including photocatalytic tests, XRD, SEM, FTIR, and PL.

Results and Discussion

Structural Analysis

Figure 1 showed the Mg metal doped ZnO sample's XRD pattern. The JCPDS file #80-0075 and the crystal planes of the wurtzite ZnO structure balanced all of the diffraction peaks. The XRD patterns of synthetic samples of Mg substituted ZnO in the range of 2θ (diffraction angle) from 10° to 90° are displayed in Figure 1, which includes all of the diffraction peaks [7]. As indicated by hkl values (100), (002), (101), (102), (103), (200), (112), (201), and (202), etc., the diffraction peaks at 2θ values 31.66°, 34.31°, 36.28°, 47.53°, 56.33°, 62.54°, 67.89°, 69.08°, 72.46°, 76.93°, and 81.48° are depicted in Figure 1.

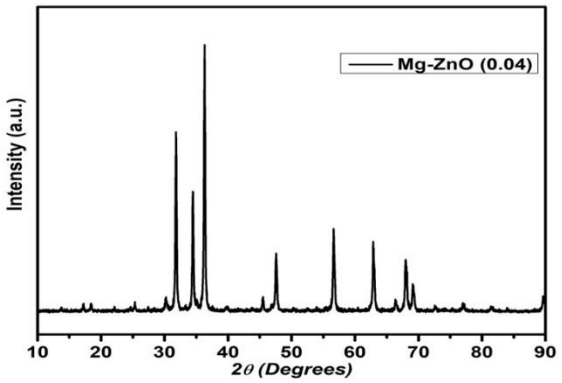

Figure 1: XRD patterns of Mg doped ZnO calcined at 450 ℃.

This demonstrated that dopant magnesium ions effectively substituted Zn^{2+} ions. No signals from secondary doped ion phases or another ZnO phase were detected. The Scherer relation can be used to measure the standard particle grain size (D).

Table 1: Pure zinc oxide with annealing and its lattice parameters

Sample	Crystallite size (nm)	Inter planar spacing (d) Å	lattice constant Å		Volume (V) Å^3	X ray Density (d_x) g/cm^3	Lattice Strain η
			a=b	c			
Mg-ZnO (0.04)	35.2	2.6122	3.5721	5.4247	60.91	8.04	0.0061

The lattice parameter of the samples was computed, and the values of 'd' were ascertained using the Bragg equation. Because of the surface aggregation of ZnO nanoparticles and the amalgamation of Mg into the lattices, the diffraction patterns of the cerium ZnO samples are nearly the same as those of nanoparticles of pure ZnO with a slight adjustment to higher 2θ angles in the peak position. This indicates that iron doping preserves the same orientations of the diffraction plane and does not change the ZnO hexagonal wurtzite structure. Furthermore, in contrast to the spiky and extremely intense peaks for the hexagonal structures, the extremely lower intensities of the diffraction crest assigned to the oxides describe the hexagonal phase of the zinc oxide lattice. Additionally, as reported by numerous other sources [8–9], the crystalline diameters decrease with Mg substitution because of the difference in the ionic radii of Mg and Zn ions. The addition of the magnesium substituent to the lattices allowed for the determination of the change in the lattice variables as measured from the XRD data. For Mg doped ZnO nanoparticles, the lattice variables a and c are 3.5721 Å and 5.4247 Å, respectively (Table 1), which are therefore close to the standards value for undoped Zinc Oxides nanoparticles (Table 1). Additionally, the c/a ratio values have been roughly constant, and they exhibit remarkable consistency with the standard values of 1.60. The Williamsons-Hall (W-H) equation [9] can be used to determine the lattice strains stimulated by the amalgamation of Mg ions into the crystals construction of Mg doped ZnO as well as the crystalline sizes. Since the crystalline sizes and strains are obtained from the Williamsons-Hall graphs, the y-intercepts provide the opposite of the crystalline sizes, and the slopes are equivalent to the strain value. Table 1 compiles the strain values and crystallite scale of zinc oxide nanoparticles, which are determined from W-H plots. Table

1 discloses the estimated cell characteristics of ZnO doped with magnesium.

Morphological Analysis

Figure 2 shows the impact of Mg ion on the morphology of ZnO when clicked out using FeSEM. Because of the massive chemical reaction of energy, the micrographs shown in the illustration are polycrystalline in nature and display agglomeration, asymmetric shapes, and sizes. The asymmetrical particle dispensation ensures that nanostructures have structural, electrical, and other properties. The XRD review also makes these findings accurate [10].

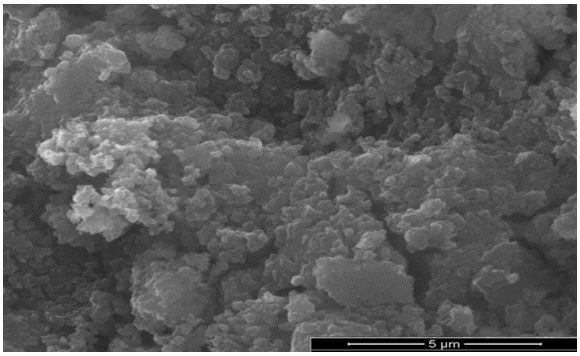

Figure 2: FESEM images of Mg doped ZnO nanoparticles calcined at 450 ℃.

PL Analysis

The photoluminescence (PL) spectra of a Mg doped ZnO sample with a purposeful excitation wavelength (λ) of 330 nm are shown in Figure 3.

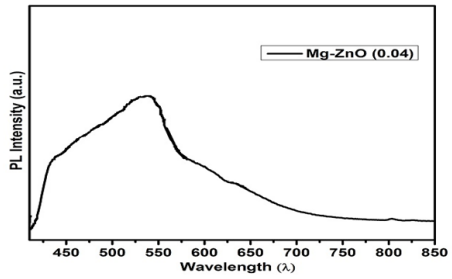

Figure 3: Photoluminescence spectrum of Mg doped ZnO nanoparticles calcined at 450 ℃.

Strong centralization of the emission peak was seen at about 435 nm, with red shifts associated with the close-band emission in zinc oxide. This is because the substitution of magnesium ions results in doped ZnO inadequacies, which may establish a negligible energy level close to the conduction bands. Therefore, the insignificant energy levels generated in the recombination centres might support the violet emissions peaks [10–11]. As a result, the adjustment of Mg led to the formation of interstitial Zn ions and oxygen vacancies, which significantly impacted the optical properties of the doping ion-modified ZnO samples.

FT-IR Analysis

The 400–4000 cm^{-1} wave range FTIR spectra of the magnesium doped ZnO sample is displayed in Figure 4.

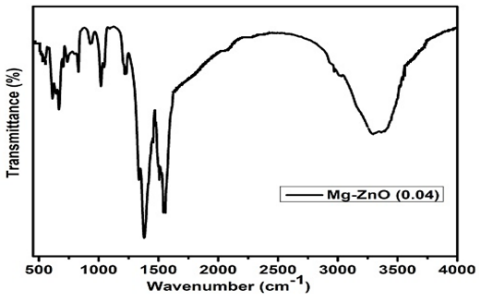

Figure 4: FT-IR Spectrum of Mg doped ZnO nanoparticles calcined at 450 ℃.

The IR pinnacles of the magnesium-doped ZnO samples are located at 3422, 2403, 1600, 1434, 1232, 843, 622, and 535 cm^{-1}. The vibrations of the C-H, C=O, and C-O bonds are represented by the FTIR peak in the range of 680 cm^{-1} to 1600 cm^{-1}. The small and jumbled absorptions band at around 843 cm^{-1} accounts for the sparse situation next to Mg in the Zn-O lattice structure. The elongation of the Zn-O bonds is reflected in peaks about 535–680 cm^{-1} [12]. The remaining peaks, which represent the O=C=O bond availabilities, submerged water mode of bending, and stretching vibrations of the O-H bond, are located between 1600 and 3422 cm^{-1}.

Photo-catalytic Test

The prepared Mg doped ZnO sample was analysed for photo-catalysis applications. The photo-catalysis experiments were conducted for the degradation of MB (methylene blue) and Malathion pesticide, in an aqueous medium in the presence of visible light. In this study, the catalytic reactor structure was set in a cubical chamber for the accomplishment of a dark medium. In a typical procedure, 50 mL of dye solution (12 mg/L) was put in a container, containing photo-catalyst (1.1 g/L). After 20 minutes of sonication, the powdered photocatalyst was fully distributed throughout the dye solution. Following this, the solution was left in the dark for 30 minutes to establish equilibrium between dye and catalyst [13]. After continuous time intervals of 20 minutes during the test run, 2–3 mL of the solution was removed and centrifuged to remove the photo-catalyst for the prescription of the dye concentration in solution using a UV-visible spectrophotometer.

Photo-catalytic studies

As said in segment 3.5, the degradation spectra of the MB dye in an aqueous solution was observed when visible light was applied in order to study the photo-catalytic investigations of the Mg doped ZnO sample. Because of the

long chromophore, the distinctive absorption peaks of MB dye are situated at approximately 662 nm. The breakdown of MB (organic pollutant) dye in the medium of a ZnO sample doped with magnesium as a photo-catalyst is shown in Figure 5 with respect to time variations.

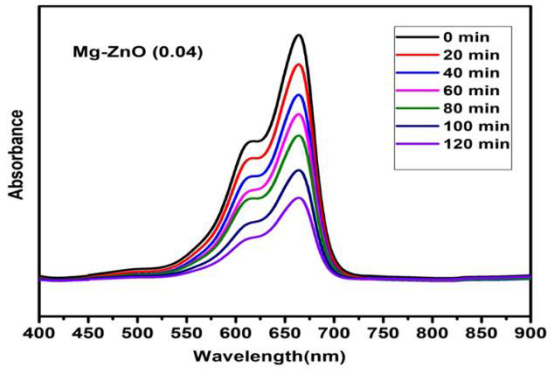

Figure 5: Photo-catalytic degradation spectrum of Mg doped ZnO nanoparticles calcined at 450℃.

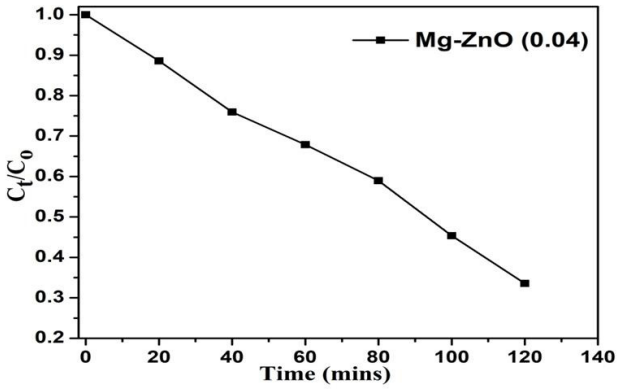

Figure 6: Variation of Ct/Co (concentration ratio) with time (min) for Mg doped ZnO nanoparticles calcined at 450 ℃

Figures 5 and 6 show how the amount of organic contaminants in water decreases, giving way to the catalyst's shape and the dye's atomic structure, among other things. Based on the relation [14], the efficiencies of degradation (η) of the BCFO photocatalysts have been estimated:

$$Degradation\ (\eta\%) = \frac{C_o - C_t}{C_o} * 100$$

where C_t is the absorbance intensity at time t = t and C_o is the initial absorbance intensity. Figure displays the changes in the comparative rates (C_t/C_o) of the ZnO sample doped with magnesium. Since the MB dye does not absorb light at a higher rate, we need a photo-catalyst nanomaterial to absorb light at unusual wavelengths (λ) in order to degrade the MB dye and remove organic contaminants from water [15]. In comparison to ZnO and many other catalysts, such as Ce-ZnO/ZnO, Ce-TiO_2/TiO_2, etc., the energy gap modification in the doped ZnO sample due to the doping of Mg is enhanced the surface reactivity because of augmenting in surface area and well crystalline character [14–17]. This reveals preferential catalysis practice under the visible light irradiation.

Photo-catalytic Mechanism

The presence of a possible catalyst, such as Mg-doped ZnO, is necessary to understand the process of photon-induced catalysis and to identify the precise mechanism involved in visible light-driven photocatalysis. Because of light absorption, light irradiation (hv ≥ Eg) on the photo-catalyst surface produces electrons-holes (e^- - h^+) in the band structure, which is crucial for the degradation of dyes or pesticides by generating hydroxyl radicals or free active radicals [17]. Furthermore, the electron smoke on the surface of the magnetic material may be the key component in the catalytic process to enhance the photo-catalytic practices in two ways: (i) the electron smoke acts as a polarised surface because of the local electric field; (ii) the rate of recombination may be significantly shortened by trapping these carriers in the electron smoke, which creates the catalyst-dye interface needed to break down the MB dye or organic pollutants from the water. The hydroxyl or free radicals (O_2^-, ^-OH, etc.) that are generated during the glibness of e^--h^+ couples via H_2O and O_2 function as an active species in photon-induced catalysis.

In the photo-catalytic process, the hydroxyl radicals or free radicals (O_{2-}, ^-OH, etc.) that are generated during the glibness of electron-hole pairs via water and oxygen function as energetic species:

$$Mg/ZnO + Photon = Mg/ZnO^* \text{ (formation of } e^- - h^+)$$

$$Mg^{3+} + e^- = Mg^{2+} \text{ } (e^- \text{ trap})$$

$$O_2 + Mg^{2+} = Mg^{3+} + O_2^-$$

$$O_2^- + H^+ = {}^{\cdot}OOH$$

$${}^{\cdot}OOH + e^-_{CB} + H^+ = H_2O_2$$

$$e^-_{CB} + H_2O_2 = {}^{\cdot}OH + {}^-OH \text{ (creation of Hydroxyl radical)}$$

$$h^+_{CB} + MB = \text{Dye Oxidized}$$

A non-toxic or innocuous substance is formed when this hydroxyl radicals/free radicals combine with the organic impurities in MB dye during the dye breakdown process.

$${}^{\cdot}OH + MB\ Dye = CO_2 + H_2O$$

$${}^{\cdot}O_2^- + MB\ Dye = H_2O + CO_2$$

It is evident from this action that pure ZnO's photocatalytic activity is significantly increased upon the addition of Mg doping content.

Conclusion

The Mg doped ZnO sample was successfully created at 450 ˚C using the co-perception technique in order to investigate the effects of Mg ions on the preparation process and its properties. The wurtzite hexagonal structure is verified by the XRD data. The computed values for the Mg doped ZnO crystallite sizes, planner distance, and cell volume are 35.2 nm, 2.6122 Å, and 60.91 $Å^3$. Agglomeration in ZnO may be seen in the FESEM photos of Mg doped ZnO. The emission wavelength (λ) is observed to be approximately 450 nm from the PL graph. The peaks in the IR spectra are located between 520 and 640 cm^{-1}, and they correspond to the Zn-O bond being stretched. Using a photocatalytic reactor, the photocatalytic degradation of magnesium-doped ZnO nanoparticles was measured for two hours. The sample of Mg-doped ZnO has a degradation efficiency (η%) of 67%, indicating its potential utility in the dye industry for purifying water.

Acknowledgement

Authors are thankful to the Department of Physics, Baba Mastnath University, Rohtak (India) for providing facilities.

References

1. M. Caglar, et al., Influence of dopant concentration on the optical properties of ZnO: In films by sol–gel method, Thin Solid Films 517.17 (2009): 5023-5028.
2. K. H. Kim, et al., A comparative study on the structural properties of ZnO and Ni-doped ZnO nanostructures,Materials Letters 149 (2015): 8-11.
3. A. Mclaren et al., Shape and size effects of ZnO nanocrystals on photocatalytic activity, Journal of the American Chemical Society 131.35 (2009): 12540-12541.
4. J. Schrier, et al., Optical properties of ZnO/ZnS and ZnO/ZnTe heterostructures for photovoltaic applications, Nano letters 7.8 (2007): 2377-2382.
5. A. S. Menon, et al., Studies on structural and optical properties of ZnO and Mn-doped ZnO nanopowders, Indian Journal of NanoScience 1.1 (2013): 16-24.
6. M. Kumar, et al., Modulation of structural properties of Sn doped ZnO for UV photoconductors, Sensors and Actuators A: Physical 270 (2018): 118-126.
7. M. Ghorbani et al., Flexible freestanding sandwich type ZnO/rGO/ZnO electrode for wearable supercapacitor, Applied Surface Science 419 (2017): 277-285.
8. M. Shafiq et al., Structural, thermal, and antibacterial properties of chitosan/ZnO composites, Polymer composites 35.1 (2014): 79-85.
9. M. Sreejesh et al., Microwave assisted synthesis of rGO/ZnO composites for non-enzymatic glucose sensing and supercapacitor applications, Ceramics International 43.6 (2017): 4895-4903.
10. N. Saha et al., Cellular proliferation, cellular viability, and biocompatibility of HA-ZnO composites, Journal of Biomedical Materials Research Part B: Applied Biomaterials 100.1 (2012): 256-264.
11. S. Wang et al., Comparison of tribological behavior of nylon composites filled with zinc oxide particles and whiskers, Wear 266.1-2 (2009): 248-254.
12. Z. Xiang et al., Efficient charge separation of Ag2CO3/ZnO composites prepared by a facile precipitation approach and its dependence on loading content of Ag2CO3, Materials Science in Semiconductor Processing 52 (2016): 62-67.
13. Z. Li et al., Improving the electric field distribution in stress cone of HTS dc cable terminals by nonlinear conductive epoxy/ZnO composites, IEEE Transactions on Applied Superconductivity 29.2 (2018): 1-5.
14. M. Cao et al., Well-organized assembly of ZnO hollow cages and their derived Ag/ZnO composites with enhanced photocatalytic property, Materials Characterization 160 (2020): 110125.
15. B. Shohany et al., Doped ZnO nanostructures with selected elements-Structural, morphology and optical properties: A review, Ceramics International 46.5 (2020): 5507-5520.
16. S. Suwanboon et al., Dependence of optical properties on doping metal, crystallite size and defect concentration of M-doped ZnO nanopowders (M= Al, Mg, Ti), Ceramics International 37.4 (2011): 1359-1365.
17. B. Y. Geng, et al., Synthesis and optical properties of S-doped ZnO nanowires, Applied Physics Letters 82.26 (2003): 4791-4793.
18. J. Yang, et al., Low-temperature growth and optical properties of Ce-doped ZnO nanorods, Applied Surface Science 255.5 (2008): 2646-2650.
19. A. Hameed et al., hotocatalytic decolourization of dyes on NiO–ZnO nano-composites, Photochemical & Photobiological Sciences 8, no. 5 (2009): 677-682.
20. G. Di et al., Targeted modulation of g-C3N4 photocatalytic performance for pharmaceutical pollutants in water using ZnFe-LDH derived mixed metal oxides: Structure-activity and mechanism., Science of The Total Environment 650 (2019): 1112-1121.
21. W. A. Sadik, et al., The Use of heterogeneous advanced oxidation processes to degrade neutral

Red Dye in aqueous solution, Polymer-Plastics Technology and Engineering 43, no. 6 (2004): 1675-1686.

22. Q. Wan et al., Enhanced photocatalytic activity of ZnO nanotetrapods, Applied Physics Letters 87, no. 8 (2005): 083105.
23. Y. H. Tan et al., MoS2@ ZnO nano-heterojunctions with enhanced photocatalysis and field emission properties, Journal of Applied Physics 116, no. 6 (2014): 064305.
24. K. Hayat, et al., Nano ZnO synthesis by modified sol gel method and its application in heterogeneous photocatalytic removal of phenol from water, Applied Catalysis A: General 393, no. 1-2 (2011): 122-129.
25. S. Payra, et al., A correlation story of syntheses of ZnO and their influence on photocatalysis, Advanced Powder Technology 31, no. 2 (2020): 510-520.

Exploring Ultrasonic Velocity and Compressibility Analysis for Various Edible Oils: A Comparative Study

M. D. Sharma

Department of Physics, Govt. Dungar College, Bikaner-334001, Rajasthan, India.

mdsharma.phy@gmail.com

Abstract

This study presents a comparative analysis of ultrasonic velocity and compressibility properties in a selection of commonly used edible oils, namely mustard oil, olive oil, coconut oil, groundnut oil, and soybean oil. Understanding the acoustic and compressibility characteristics of these oils is of significant interest due to their widespread culinary and industrial applications. Ultrasonic velocity measurements were conducted using a precision ultrasonic velocity analyzer, while compressibility analysis was performed through precise density measurements. Our findings reveal distinct differences in ultrasonic velocity and compressibility among the various oils. This comparative study contributes to our understanding of the acoustical and compressibility characteristics of edible oils, offering potential applications in food processing, quality control, and product development. Additionally, the findings may have implications in the field of biomedical and industrial applications where these oils are utilized.

Keywords: Edible Oils, Compressibility, Ultrasonic Velocity.
Received 05 April 2024; First Review 12 April 2024; Accepted 12 April 2024.

*** Address of correspondence**
Dr. M. D. Sharma
Department of Physics, Govt. Dungar College, Bikaner-334001, Rajasthan, India.

Email: mdsharma.phy@gmail.com

How to cite this article
M. D. Sharma, Exploring Ultrasonic Velocity and Compressibility Analysis for Various Edible Oils: A Comparative Study, J. Cond. Matt. 2024; 02 (01): 17-20.

Available from:
https://doi.org/10.61343/jcm.v2i01.50

Introduction

Edible oils are essential components of our daily diet and play a pivotal role in culinary practices worldwide. Beyond their culinary significance, these oils are also widely used in various industrial applications, making their characterization and understanding of their physical properties crucial. One such aspect of interest is the exploration of ultrasonic velocity and compressibility in different edible oils. Ultrasonic velocity, the speed at which sound travels through a medium, and compressibility, a measure of how a substance responds to changes in pressure, are fundamental physical properties. In the context of edible oils, these properties can provide valuable insights into their composition, structure, and potential applications.

This study aims to delve into the ultrasonic velocity and compressibility [1-2] characteristics of a selection of commonly consumed edible oils, including mustard oil, olive oil, coconut oil, groundnut oil, and soybean oil. While these oils share the commonality of being edible, they also exhibit distinct chemical compositions, fatty acid profiles, and sensory attributes. Understanding the acoustical and compressibility properties of these oils can shed light on their unique characteristics and applications. Ultrasonic velocity analysis allows us to investigate the speed at which sound waves propagate through each oil, providing information about their density and compressibility. Compressibility, on the other hand, informs us about the oil's ability to be compressed under pressure, which is relevant for various industrial processes.

In this paper, our focus centres on the fundamental physical properties of various edible oils at room temperature. Specifically, we delve into the ultrasonic velocity (u), compressibility (β), and bulk modulus (μ) [3-6] of these oils. These properties are pivotal in understanding the behavior of edible oils, both in culinary contexts and across a spectrum of industrial applications.

Experimental

Material

In this comprehensive study, the focus was on the analysis of five widely consumed edible oils: mustard oil, soybean oil, olive oil, coconut oil, and groundnut oil. The selection of these oils was deliberate, aiming to encompass a broad spectrum of culinary and industrial applications. Each of these oils possesses unique characteristics that make them significant in various culinary traditions and industrial processes.

Mustard oil, known for its pungent taste, is commonly used in Indian and South Asian cuisines. Soybean oil, a versatile and neutral-flavored oil, finds extensive use in both cooking and as an industrial ingredient. Olive oil, renowned for its health benefits and distinct taste, is a staple in Mediterranean cooking. Coconut oil, with its tropical aroma and versatility, has a wide range of applications, from cooking to cosmetics. Groundnut oil, often used for its high smoke point and mild taste, is popular in frying and sautéing.

By analyzing these oils, this study provides insights into their nutritional content, flavor profiles, and physical properties, offering valuable information for both consumers and industries seeking to make informed choices regarding these essential food ingredients.

Procedure

In this scientific investigation, ultrasonic velocities in liquid mixtures were meticulously assessed using a specialized methodology. Ultrasonic sound pertains to acoustic waves with frequencies exceeding the range of human audibility, typically falling within the domain of 20 Hz to 20 KHz. When an ultrasonic wave traverses through a medium, it triggers minute vibrational movements among the constituent molecules. These vibrations are parallel to the longitudinal wave's direction, facilitating the exchange of momentum between the molecules. This molecular interaction allows the ultrasonic wave to propagate through the medium, providing valuable insights into the medium's acoustic properties and behavior.

To execute these measurements with precision, a single crystal ultrasonic interferometer was employed. This sophisticated apparatus comprises a high-frequency generator and a measuring cell, guaranteeing the accuracy of ultrasonic velocity assessments. The measurements in this study were performed at a fixed frequency of 2 MHz, ensuring consistent and controlled conditions for the experiments.

By quantifying ultrasonic velocities in liquid mixtures, this research contributes to a deeper understanding of the acoustic characteristics and molecular dynamics within these mixtures. Such knowledge has far-reaching implications, including the optimization of industrial processes, the development of novel materials, and advancements in various scientific fields.

The experimental values of velocity, compressibility and Bulk modulus are calculated by using the following standard relations; Adiabatic compressibility [3],

$$\beta = 1/\rho u^2 \qquad (1)$$

where ρ is the density of oil and u is the ultrasonic velocity.

Bulk modulus [4-5],

$$\mu = 1/\beta \qquad (2)$$

Results and Discussion

The study has undertaken the measurement of ultrasonic velocity in a range of edible oils using an ultrasonic interferometer. The data collected includes observed values of ultrasonic velocity (u), compressibility (β), and bulk modulus (μ) for the oil samples at different levels of contraction, which are presented in Table 1. This data is invaluable in providing insights into the acoustic properties and behavior of these edible oils under various conditions.
Ultrasonic velocity measurements offer essential information regarding the speed of sound propagation through the oils, which can be indicative of their molecular interactions and physical properties. Compressibility and bulk modulus data are fundamental for characterizing the oils' responses to changes in pressure, indicating their compressibility and elasticity.

This dataset forms the cornerstone of the study, likely serving as a basis for understanding the behavior of different edible oils under varying conditions. Furthermore, it can have practical applications in industries that involve the use of these oils, such as food processing and biofuel production, aiding in optimizing processes and product formulations.

In the initial phase of our experiment, soybean oil was used as the experimental liquid in the ultrasonic interferometer to measure the velocity of ultrasonic waves at a frequency of 2 MHz. The known density of soybean oil, which is 909.97 kg/m³, was a crucial parameter for these measurements. In this particular case, the velocity of the ultrasonic wave in soybean oil was observed to be 1407.21 m/s.
Building on this approach, the study extended to include a variety of other edible oils, such as groundnut oil, mustard oil, olive oil, coconut oil, and sesame oil. For each of these oils, their respective densities and ultrasonic wave velocities were measured and recorded. The resulting data, as presented in Table 1, forms a comprehensive set of information regarding the acoustic properties of these edible oils.

This systematic approach allows for a comparative analysis of ultrasonic properties among different edible oils, shedding light on their acoustic behavior and providing valuable data for a range of applications, including food science, processing, and quality control. The combination of density and ultrasonic velocity measurements offers insights into the unique physical characteristics of each oil, contributing to a deeper understanding of their properties and potential uses in various industrial and culinary applications.

The table provides essential data on various edible oils, showcasing their physical and acoustic properties. Here's a discussion of the key findings:

The density values of these edible oils range from 909.97 kg/m³ for soybean oil to 920.00 kg/m³ for olive oil. Density is an important parameter, as it influences the buoyancy, viscosity, and overall physical behavior of these oils. Olive oil, with the highest density, is relatively denser than the others.

Table 1: Density, Ultrasonic velocity, Compressibility and Bulk Modulus for various edible oils at room temperature.

Edible Oil	Density (kg/m³)	Ultrasonic Velocity (m/s)	Compressibility (β) in 10^{-10} (m²/N)	Bulk Modulus (μ) in 10^{10} (N/m²)
Soybeans Oil	909.97	1407.21	5.5495	0.1802
Groundnut Oil	910.00	1410.07	5.5268	0.1809
Mustard Oil	910.00	1497.23	4.9021	0.2040
Olive Oil	920.00	1397.24	5.5676	0.1796
Coconut Oil	914.28	1368.28	5.8421	0.1712
Sesame Oil	910.00	1388.92	5.6964	0.1755

Ultrasonic velocity measures the speed of sound propagation through the oils. Mustard oil demonstrates the highest ultrasonic velocity at 1497.23 m/s, indicating its efficient transmission of sound waves. Coconut oil, on the other hand, has the lowest ultrasonic velocity, suggesting slower sound propagation.

Compressibility measures the oils' ability to change volume under the influence of pressure. Mustard oil, with the lowest compressibility value (4.9021 x 10^{-10} m²/N), is the least compressible. Groundnut oil, with a slightly higher value, is relatively more compressible.

Bulk modulus quantifies the oils' resistance to compression. Mustard oil, with a higher bulk modulus value (0.2040 x 10^{10} N/m²), is the most resistant to compression. Coconut oil, with the lowest value, is relatively less resistant.

This data is significant in various fields, including food processing, where these oils are utilized, and in industrial applications. It aids in selecting the right oil for specific applications and optimizing processes. Each oil's unique combination of properties makes it suitable for various culinary and industrial uses.

Conclusion

In conclusion, the provided data on different edible oils, including their density, ultrasonic velocity, compressibility, and bulk modulus, offers valuable insights into their diverse physical and acoustic properties. These findings have significant implications for various applications, including food preparation, industrial processes, and material selection.

Density: The density of these oils varies, with olive oil being the densest and soybean oil the lightest. This difference in density can affect their behavior in culinary applications and their ability to mix with other ingredients.

Ultrasonic Velocity: The ultrasonic velocity data demonstrates that each oil transmits sound waves at different speeds. Mustard oil is the fastest, while coconut oil is the slowest. This property can impact their acoustic behavior and suitability for certain uses.

Compressibility and Bulk Modulus: Compressibility and bulk modulus data provide insights into how these oils respond to changes in pressure. Mustard oil is the least compressible and most resistant to compression, while coconut oil is relatively more compressible and less resistant. These properties have implications for processes like frying and extraction.

In practical terms, this information assists in selecting the right oil for specific culinary and industrial applications. It allows for informed choices based on the unique properties of each oil, ultimately contributing to the optimization of processes and product formulations. This data is a valuable resource for researchers, food scientists, and industries seeking to understand and utilize these edible oils effectively.

References

1. S. L. Oswel, P. Oswel, R. P. Phalak, J. Sol. Chem. 27 (1998) 507.
2. J. Rajasekhar, P. Naidu, J. Chem. Eng. Data 41(1996) 373.
3. M. Kalidoss, R. Srnivasamoorthy, J. Pure Appl. Ultrason. 19 (1997) 9.
4. W. Boch, P. Miecznik, Acoustics Lett. 10 (1986) 74.
5. P. Subramanyam Naidu, K. Ravindra Prasad, J. Pure Applied Ultrason. 27 (2005) 15.

K. Narendra, Ch. Srinivasu, Sk. Fakruddin, P. Narayanamurthy, J. Chem. Thermodyn. 43 (2011) 1604.

Study of perylene Di-imide as a Binder of a Human Telomeric Tetraplex DNA by Molecular Docking Simulation

Vandana Mishra[a], Rakesh Kumar Tiwari[b]

Department of Physics, D.D.U. Gorakhpur University, Gorakhpur U.P, India.

[a] vandnam149@gmail.com
[b] drrkt@yahoo.com

Abstract

Human telomeres are consisting of d(TTAGGG) repeats involved in the formation of tetraplex DNA structures. Ligands stabilizing these tetraplex DNA structures are potential inhibitors of the cancer cell-associated enzyme telomerase. In human cells, telomerase adds multiple copies of the 5'-GGTTAG-3' motif to the end of the G-strand of the telomere and in the majority of tumour cells it results over-expressed. Several structural studies have revealed a diversity of topologies for telomeric tetraplexes, which are sensitive to the nature of the cations present, to the flanking sequences, and probably also to concentration, as confirmed by the different conformations deposited in the Protein Data Bank (PDB). The existence of different polymorphism in the DNA quadruplex and the absence of a uniquely precise binding site give rise to a better understanding of mechanism by verifying with docking methodology approach. To target this, we have selected six different experimental models of the human telomeric sequence d[AG3(T2AG3)3] with the ligands (the perylene di-imide). We simulated out molecular docking of binding of perylene di-imide to a selected G-quadruplex using dock 6.9 to examine the or loop binding mode of perylene di-imide.

The simulation provides the two highest rank docking poses of perylene di-imide i.e. with external strand and groove binding mode; the role different ligand binding is described as external striking on the terminal guanine tetrad and the groove binding. which may be further considered for the study of therapeutic properties of ligand.

Keywords: DNA Duplex, Docking, Telomeric Quadruplex and Molecular Interaction.
Received 06 February 2024; First Review 02 April 2024; Accepted 22 April 2024.

*** Address of correspondence**
Vandana Mishra
Department of Physics, D.D.U. Gorakhpur University, Gorakhpur U.P, India.

Email: vandnam149@gmail.com

How to cite this article
Vandana Mishra, Rakesh Kumar Tiwari, Study of perylene Di-imide as a Binder of a Human Telomeric Tetraplex DNA by Molecular Docking Simulation, J. Cond. Matt. 2024; 02 (01): 20-23.

Available from:
https://doi.org/10.61343/jcm.v2i01.49

Introduction

G-tetraplex DNA is a high concentration structure of G-Prosperity nucleic acid sequence. They are held together by a hoogesteen type of hydrogen bond and stabilized by monovalent cations [1]. These structures are found at the ends of eukaryotic chromosomes and-MYC, C-kit, KRAS and BCL-2 Such as are found in affected areas called promoter region [2]. G-tetraplex structures may also play a role in the translation process, which are potentially present in messenger RNA. Stable tetraplex has been shown to effectively prevent telomerase activation, which is often overexpressed in human cancers [3].

In solution four-Repetitive human telomere sequences, d[AG3(T2AG3)3], first of NMR-Characteristics of based structure1993 Was made in [4]. This sequence is an intramolecular-forms G-quadruplex in which three stacked G-Tetrads are involved with anti Syn-Syn around each tetrad glycosidic structure. The adenine bases of loop Through stacking interactions with G-tetrads let's talk, a so-called basket structure(pdb143D) [5].

In 2002, By Professor Needle's group in a K^+ the different sequence of the same sequence in the compound crystal [6]. G- quadruplex structure was observed: all four strands are parallel, Connecting TTA loop double chain-are reversers, and all guanine based Let's adopt anti- glycosidic structure (pdb1KF1), Later studies physiological K^+ for several human telomere sequences in solution conditions Indicated the presence of a mixture of G- quadruplex forms [7].

Other than this, NMR analysis revealed that the telomeric sequence contains other intramolecular conformations, which are defined as hybrids. Small ligands can promote the formation of quadruplex structures from telomeric DNA, can inhibit telomerase enzyme and cause telomere ends in cancer cells, may destabilize end-capping [8]. Based on this,

Design of new ligands as potential anticancer agents. Several studies have been conducted to synthesize and evaluate G-quadruplex ligands as potential anti-cancer agent [9].

In this perspective, we come across a website on which structure of many drugs were made. from here we downloaded the structure of perylene di-imide [PDIs] and got it docking simulation with human telomeric sequence d[AG3(T2AG3].

Perylene Di-imide (PDIs)

The structure of perylene di-imide is shown in figure 1.

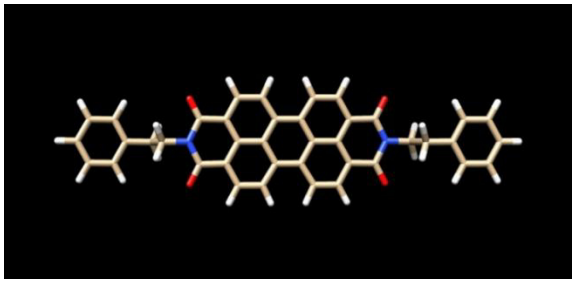

Figure 1: perylene di-imide

Perylene di-imide is also known as N-N di-(2phenylethyl) perylene carbonic acid, amide. Molecular formula is C40H26N2O4 [PUBCHEM]. PDIs are highly electron deficient conjugated structure that can exist stably in ambient environments. PDIs also targets binding of terminal telomeric G-quadruplex inhibiting telomerase [10].

Methodology

Receptor preparation

Downloaded structures from the Protein Data Bank (PDB) including 1KF1, 4wo3, and NMR models 143d, 2l7v, 2mb3, 2mgn, and 2o3m related to the telomeric sequence d[AG3(T2AG3)3] underwent pre-treatment. Co-crystallized water molecules and counter ions were removed from these structures. Additionally, any sequences containing hybrid models were noted to have head and tail caps, each consisting of a different number of additional nucleotides.

Ligand preparation

The perylene di-imide depicted in figure 1 was utilized in the current study. The ligand structure was obtained by downloading it from the PUBCHEM website. Subsequently, the structure with the lowest energy conformation was selected. This chosen conformation was then prepared for further docking studies, maximizing torsion, using the dock 6.9 tool.

Docking Conditions

In the final step, the docking approaches employed involved screening all generated configurations. Configurations within 3 kcal mol^{-1} above the global minimum energy complex were subjected to full minimization using the same force field and environment described for the target optimization procedure. Analysis of the results incorporated consideration of thermodynamic estimates derived from state equations, including free energy, enthalpy, and entropy of complex formation computed at 300 K.

Three-dimensional figures were generated using CHIMERA graphics, as depicted below. All calculations were executed on a Linux cluster.

Results and Discussion

Considering this observation, we decided to include it in the docking analysis with the widely used method Dock 6.9. The human telomeric repeat sequence, d[AG3(T2AG3)3], has been experimentally characterized in various conformations. To account for conformational variability, we included six PDB models (1kf1, 2L7v, 2mgn, 2o3m, 4wo3, 143d, 2mb3) representing both X-ray and NMR structures, specifically on G-tetrad structures be focused shown in figure 2.

(a): 1kf1.pdb

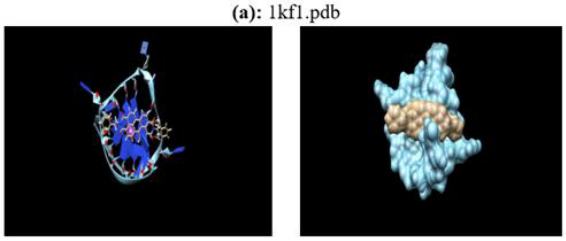

(b): 2l7v.pdb

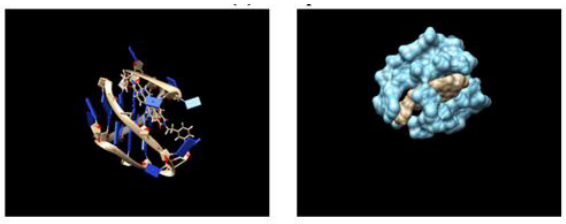

(c): 2mgn.pdb

(d): 2o3m.pdb

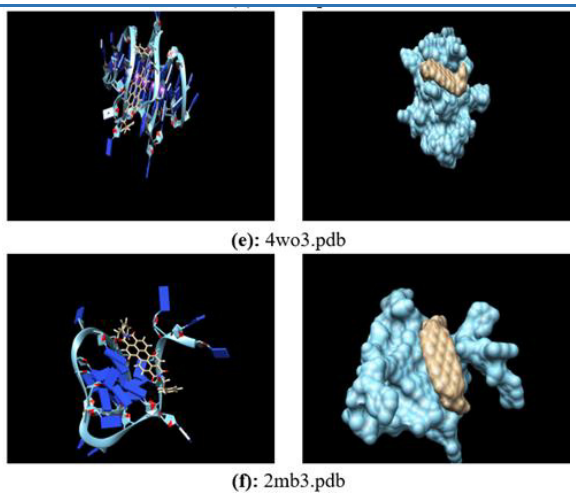

(e): 4wo3.pdb

(f): 2mb3.pdb

Figure 2: Six PDB models representing both X-ray and NMR structures.

Evaluation of the most stable conformations for each model was conducted after the pretreatment, which included structural optimization through energy minimization. Below is included an image showing various G-Tetraplex complexes with perylene di-imide. In each displayed image, the view on the left presents the standard perspective provided by the CHIMERA software, while the view on the right presents a surface view also generated by CHIMERA. The depicted images depict complex structures, where the sky-blue colour represents the receptor and the brown colour represents the ligand, specifically perylene di-imide.

Table 1: Docking energy score (score), van der Waal energy (VDW) and electrostatic energy (ES) (kcl/mol) in perylene di-imide /G-quadruplex complex

PDB ID	Flexible Docking			Rigid Docking		
	Grid Score	VDW	ES	Grid Score	VDW	ES
1kf1.PDB	-52.8227	-53.3581	0.5343	-38.1245	-38.6771	0.5525
2l7v.PDB	-54.9683	-55.8302	0.8619	-61.3475	-60.7928	-0.5546
2mgn.PDB	-58.3899	-57.6830	-0.7068	-47.3569	-46.0942	-1.2626
2o3m.PDB	-48.8248	-47.9873	-0.8374	-40.8491	-40.5808	-0.2683
4wo3.PDB	-42.1848	-38.7875	-3.3972	-28.2489	-28.6594	0.4104
2mb3.PDB	-48.7457	-48.7259	-0.0215	-40.6448	-41.8792	1.2344

Conclusion

In conclusion, we modelled the G-tetraplex fold, using experimentally described conformations of the human telomeric repeat sequence d[AG3(T2AG3)3] based on the six G-tetrads available in protein data bank (PDB), The importance of considering diverse forms has been underlined. The chemical compound chosen as our ligand is PDIs.

Our primary motivation for conducting this study was to investigate whether molecular docking simulations using Docked 6.9 could recapitulate the binding mode observed in the crystal structure of the human telomeric G-quadruplex with PDIs.

Our molecular docking simulations generated different binding modes, both flexible and rigid in nature. The corresponding docking poses are illustrated in the figures, and the docking results are summarized in table 1. The presented docking energy scores represent the cumulative values of Vander Waals (VDW) and electrostatic (ES) terms.

References

1. Alcaro S, Costa G, Distinto S, Moraca F, Ortuso F, Parrotta L, Artese A. *The polymorphisms of DNA G-quadruplex investigated by docking experiments with telomestatin enantiomers*. Curr Pharm Des. 2012; 18(14):1873-9. https://doi.org/10.2174/138161212799958495. PMID: 22376115.
2. Routh ED, Creacy SD, Beerbower PE, Akman SA, Vaughn JP, Smaldino PJ. *A G-quadruplex DNA-affinity Approach for Purification of Enzymatically Active G4 Resolvase1*. J Vis Exp. 2017 Mar 18;(121):55496. https://doi.org/10.3791/55496. PMID: 28362374; PMCID: PMC5409278.
3. Largy E, Mergny JL, Gabelica V. *Role of Alkali Metal Ions in G-Quadruplex Nucleic Acid Structure and Stability*. Met Ions Life Sci. 2016; 16:203-58. doi:10.1007/978-3-319-21756-7_7.PMID: 26860303.
4. Sundquist WI, Klug A. *Telomeric DNA dimerizes by formation of guanine tetrads between hairpin loops. Nature*. 1989 Dec 14; 342(6251):825-9. doi:

10.1038/342825a0. PMID: 2601741.

5. Sen, D., Gilbert, W. *Formation of parallel four-stranded complexes by guanine-rich motifs in DNA and its implications for meiosis*. Nature 334, 364–366(1988). https://doi.org/10.1038/334364a0.
6. Rawal P, Kummarasetti VB, Ravindran J, Kumar N, Halder K, Sharma R, Mukerji M, Das SK, Chowdhury S. *Genome-wide prediction of G4 DNA as regulatory motifs: role in Escherichia coli global regulation*. Genome Res. 2006 May; 16(5):644-55. doi:10.1101/gr.4508806. PMID: 16651665; PMCID: PMC1457047.
7. Faure-Perraud A, Métifot M, Reigadas S, et al. *The guanine-quadruplex aptamer 93del inhibits HIV-1 replication ex vivo by interfering with viral entry, reverse transcription and integration*. Antiviral Therapy.2011;16(3):383-394. https://doi.org/10.3851/IMP1756.
8. Feuerhahn S, Iglesias N, Panza A, Porro A, *Lingner J. TERRA biogenesis, turnover and implications for function*. FEBS Lett. 2010 Sep 10; 584(17):3812-8. https://doi.org/10.1016/j.febslet.2010.07.032. Epub 2010 Jul 23. PMID: 20655916.
9. Folini M, Pivetta C, Zagotto G, De Marco C, Palumbo M, Zaffaroni N, Sissi C. *Remarkable interference with telomeric function by a G-quadruplex selective bisantrene regioisomer. Biochem Pharmacol*. 2010 Jun 15; 79(12):1781-90. https://doi.org/10.1016/j.bcp.2010.02.018.Epub 2010 Mar 3. PMID: 20206144.
10. Sponer J, Cang X, Cheatham TE 3rd. *Molecular dynamics simulations of G-DNA and perspectives on the simulation of nucleic acid structures*. Methods. 2012 May; 57(1):25-39. https://doi.org/10.1016/j.ymeth.2012.04.005.Epub 2012 Apr 16. PMID: 22525788; PMCID: PMC3775459.

Synthesis and Luminescence Studies of Eu^{2+} doped $MgSiO_3$ Inorganic Phosphors for Energy Storage Phosphors

Amol Nande

Guru Nanak College of Science, Ballarpur

Abstract

The inorganic luminescence materials are widely studies for several applications including displays, light emitting didoes, energy storage etc. In this research work, the authors have synthesized $MgSiO_3:Eu^{2+}$ inorganic phosphor using modified solid state reaction method. The prepared samples were sent for photoluminescence to study emission and excitation properties. The emission and excitation properties show broad peak which are suitable for long lasting luminescence behaviour. Thus, this material can be a good candidate for energy or data storage material. Along with experimental measurements, the emission spectra can be stimulated suing theoretical model. The both emission spectra matched with each other.

Keywords: Luminescence, Eu^{2+}, EVI parameter, Silicates.
Received 02 February 2024; First Review 05 March 2024; Accepted 25 March 2024

*** Address of correspondence**
Dr. Amol Nande
Assistant Professor, Department of Physics
Guru Nanak College of Science, Ballarpur, India

Email: nande.av@gmail.com

How to cite this article
Amol Nande, Synthesis and Luminescence Studies of Eu2+ doped MgSiO3 Inorganic Phosphors for Energy Storage Phosphors, J. Cond. Matt. 2024; 02 (01):24-26

Available from:
https://doi.org/10.61343/jcm.v2i01.141

Introduction

Luminescent materials are the inorganic and organic materials which are the combination of host compound and dopant materials [1]. These materials produce light energy under the excitation of external source like light or electricity [1]. These materials are referred as phosphors. These materials are highly used in LEDs, lasers, displays, pharmaceuticals etc [2, 3]. The rare-earth materials like Ce^{3+} and Eu^{2+} are very sensitive to around crystal field environment and produce broad emission under the excitation of particular wavelength [4, 5]. The emission of Eu^{2+} doped inorganic phosphors is generally due to the parity allowed 4f-5d transitions. Also, persistent or broad emission inorganic phosphors always have strong quantum yield value and high storage capacity [6]. Thus, these materials show prominent applications in the field of energy storage.

Terraschke et al. [6] provide a detail review based on 321 research paper and suggest that Eu^{2+} ions have electron transition between $4f^6$ to $4f^7$ energy states which are strongly influenced by host lattice. Thus, Eu^{2+} based inorganic phosphors open for many applied applications. Wang et al. [7] studied $LaSrAl_2O_3:Eu^{2+}$ inorganic phosphors and suggests the phosphor can be a good material for optical storage device. Li et al. [8] synthesized $SrAl_2O_4:Eu^{2+}$, Dy^{3+} inorganic phosphors and study the effect of Pb^{2+} ions on them. The work suggests that the material can be a promising material for information storage applications.

In this work, we synthesized $MgSiO_3:Eu^{2+}$ compound using modified solid state reaction method. The excitation and emission spectra for the sample have been studied. Further, the theoretical emission spectra are stimulated using Electronic-Vibrational Interacting parameters.

Method and Synthesis

All starting reactants for the preparation of $MgSiO_3:Eu^{2+}$ inorganic phosphors were analytical reagent grade. The inorganic phosphor was prepared using modified solid-state reaction method. The phosphor was obtained using magnesium carbonate ($MgCO_3$), silicic acid ($SiO_2.9H_2O$) and Eu_2O_3 in HNO_3 as raw materials. All stoichiometrically weighed out materials were mixed together and crushed for an hour. The mixture later heated to 800 °C for 6 hours; after 6 hours the mixture cooled down and crushed for another one hour. Afterwards, the mixture gain heated for 900 °C for 12 hours. After 12 hours, the sample kept for cooling to reach to room temperature. Once sample reached to room temperature it crushed for another hours using mortar pastel and powder sent for characterizations.

Result and Discussion

The excitation spectrum for the phosphor is measured for

456 nm emission wavelength, as shown in Figure 1 (black lines). The observed broad excitation spectrum observed between 260 nm to 400 nm. The observed excitation peak was centered at 329 nm which corresponds to ($^8S_{7/2}$) $4f^7$ ground state → $4f^65d^1$ Excited state [9, 10]. The broad excited band suggests the phosphor can be excited using near-Ultra Violet wavelength. It further suggests that Eu^{2+} is the only luminescent center and occupied the same sites in the lattice producing symmetry excited peaks.

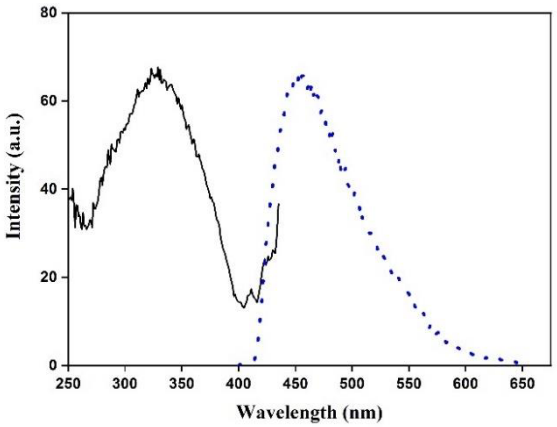

Figure 1: Excitation and emission spectra of $MgSiO_3:Eu^{2+}$ inorganic phosphor

The emission spectrum for the phosphor is measured for 329 nm excited wavelength, as shown Figure 2 (blue dotted line). The emission spectrum showed a broad peak between 410 nm to 650 nm and the peak centered at 456 nm. The emission observed in blue region corresponding to $4f^65d$ configuration to the $^8S_{7/2}$ level of the electronic configuration.

The experimental emission graph can be stimulated by calculating electron-vibrational interaction parameters such as stokes shift, Huang-Rhys factor, effective phonon energy and zero phono line position [11, 12]. The parameters ultimately used to stimulate emission parameter using following equation [13] –

$$I = \frac{e^{-S}S^m}{m!}\left(1 + S^2\frac{e^{\frac{\hbar w}{kT}}}{m+1}\right)$$

$$m = \frac{\Delta E}{\hbar w}; \Delta E = E_0 - E$$

Here, m is the effective number of phonons occurred during emission transition. E_0 is the zero-phonon energy. S is Huang-Rhys coupling constant. $\hbar$, w, k, T, and E are Plank's constant, angular velocity, Boltzmann constant, temperature, and energy at a given wavelength respectively. The stimulated emission peak is shown in Figure 2.

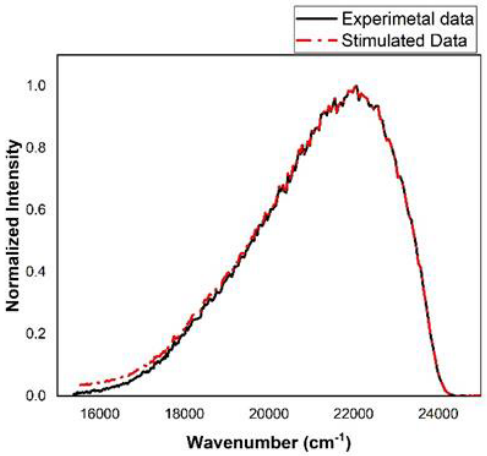

Figure 2: Experimental and stimulated emission spectra for $MgSiO_3:Eu^{2+}$ inorganic phosphor

The estimated value of S and $\hbar w$ are 2.71 and 758 cm^{-1}, respectively. From figure it is clear that there is a good matched with experimental and stimulated data.

Conclusion

The synthesized $MgSiSO_3:Eu^{2+}$ inorganic phosphors successfully made using modified solid state reaction method. The excitation and emission spectra confirmed the luminescence was due to Eu^{2+} rare-earth metal ions. The excitation spectrum was broad and was due to $^8S_{7/2}$ state → $4f^65d^1$ state and emission spectrum was also broad which was due to $4f^65d^1$ state → $^8S_{7/2}$ transition. This confirms the doping occurred in the phosphor successfully. Further, the electron-vibration interaction study showed that the experimental emission spectrum can be stimulated using theoretical model. This phosphor shows promising results and can be used for LEDs and storage devices.

Acknowledgement

The author like to thank Gondwana University, Gadchiroli for providing fund to carry out present research work under minor research scheme (reference letter No. /GUG/DIIL/612/2020).

References

1. G. Blasse, *"The physics of new luminescent materials",* Materials chemistry and physics, vol. 16, pp. 201-236, 1987.
2. C. Ronda, *"Challenges in application of luminescent materials, a tutorial overview (invited review)",* Progress In Electromagnetics Research, vol. 147, pp. 81-93, 2014.
3. C. Zhang and J. Lin, *"Defect-related luminescent materials: synthesis, emission properties and applications",* Chemical Society Reviews, vol. 41, pp. 7938-7961, 2012.

4. S. Wang, Z. Song, Y. Kong, and Q. Liu, *"Relationship of Stokes shift with composition and structure in Ce^{3+}/Eu^{2+}-doped inorganic compounds",* Journal of Luminescence, vol. 212, pp. 250-263, 2019.
5. D. Geng, M. Shang, Y. Zhang, H. Lian, and J. Lin, *"Color-tunable and white luminescence properties via energy transfer in single-phase $KNaCa_2(PO_4)_2$: A (A= Ce^{3+}, Eu^{2+}, Tb^{3+}, Mn^{2+}, Sm^{3+}) phosphors",* Inorganic chemistry, vol. 52, pp. 13708-13718, 2013.
6. H. Terraschke and C. Wickleder, *"UV, Blue, Green, Yellow, Red, and Small: Newest Developments on Eu^{2+}-Doped Nanophosphors",* Chemical Reviews, vol. 115, pp. 11352-11378, 2015/10/28 2015.
7. B. Wang, H. Wang, J. Huang, J. Zhou, and P. Liu, *"Trap distribution and photo-stimulated luminescence in $LaSrAl_3O_7:Eu^{2+}$ long-lasting phosphors for optical data storage,"* Journal of the American Ceramic Society, vol. 103, pp. 315-323, 2020.
8. P. Li, Y. Tian, F. Huang, L. Lei, M. Cai, S. Xu, et al., *"Highly efficient photo stimulated luminescence of Pb^{2+} doped $SrAl_2O_4:Eu^{2+}$, Dy^{3+} borate glass for long-term stable optical information storage",* Journal of the European Ceramic Society, vol. 42, pp. 5065-5073, 2022/09/01/ 2022.
9. K. N. Shinde, *"Luminescence in Eu^{2+} and Ce^{3+} doped $SrCaP_2O_7$ phosphors",* Results in Physics, vol. 7, pp. 178-182, 2017/01/01/ 2017.
10. H.-S. Roh, S. Hur, H. J. Song, I. J. Park, D. K. Yim, D.-W. Kim, et al., *"Luminescence properties of $Ca_5(PO_4).2SiO_4:Eu^{2+}$ green phosphor for near UV-based white LED",* Materials Letters, vol. 70, pp. 37-39, 2012/03/01/ 2012.
11. S. A. Pardhi, G. B. Nair, R. Sharma, and S. Dhoble, *"Investigation of thermoluminescence and electron-vibrational interaction parameters in $SrAl_2O_4$: Eu^{2+}, Dy^{3+} phosphors",* Journal of Luminescence, vol. 187, pp. 492-498, 2017.
12. P. D. Bhoyar and S. Dhoble, *"Study of electron vibrational interaction parameters in chlorophosphate activated with Eu^{2+} ion,"* Materials Chemistry and Physics, vol. 147, pp. 488-491, 2014.
13. A. R. Kadam, G. C. Mishra, M. Michalska-Domanska, and S. Dhoble, *"Theoretical analysis of electron vibrational interaction (EVI) parameters in 5d states of Eu^{2+} activated $BaSiF_6$ downconversion phosphor",* Journal of Molecular Structure, vol. 1229, p. 129505, 2021.